ELECTRO-OPTICS

The Infrared &
Electro-Optical
Systems Handbook

ERRATA FOR

THE INFRARED & ELECTRO-OPTICAL SYSTEMS HANDBOOK

8-VOLUME SET

TABLE OF CONTENTS

Library of Congress Cataloging-in-Publication Data

The Infrared and electro-optical systems handbook / Joseph S. Accetta,
David L. Shumaker, executive editors.
p. cm.
Spine title: IR/EO systems handbook.
Cover title: The Infrared & electro-optical systems handbook.
Completely rev. ed. of: Infrared handbook. 1978
Includes bibliographical references and indexes.
Contents: v. 1. Sources of radiation / George J. Zissis, editor —
v. 2. Atmospheric propagation of radiation / Fred G. Smith, editor —
v. 3. Electro-optical components / William D. Rogatto, editor —
v. 4. Electro-optical systems design, analysis, and testing /
Michael C. Dudzik, editor — v. 5. Passive electro-optical systems /
Stephen B. Campana, editor — v. 6. Active electro-optical systems /
Clifton S. Fox, editor — v. 7. Countermeasure systems / David Pollock, editor —
v. 8. Emerging systems and technologies / Stanley R. Robinson, editor.
ISBN 0-8194-1072-1
1. Infrared technology—Handbooks, manuals, etc.
2. Electrooptical devices—Handbooks, manuals, etc. I. Accetta, J.
S. II. Shumaker, David L. III. Infrared handbook. IV. Title:
IR/EO systems handbook. V. Title: Infrared & electro-optical
systems handbook.
TA1570.I5 1993
621.36'2—dc20 92-38055
CIP

Copublished by

Infrared Information Analysis Center
Environmental Research Institute of Michigan
P.O. Box 134001
Ann Arbor, Michigan 48113-4001

and

SPIE Optical Engineering Press
P.O. Box 10
Bellingham, Washington 98227-0010

Second (revised) printing 1996

PRINTED IN THE UNITED STATES OF AMERICA

Copublished by

ERIM

Infrared Information Analysis Center
Environmental Research Institute of Michigan
Ann Arbor, Michigan USA

and

SPIE Optical Engineering Press
Bellingham, Washington USA

Sponsored by

Defense Technical Information Center, DTIC-AI
8725 John J. Kingman Road, Suite 0944
Ft. Belvoir, Virginia 22060-6218

Directly involved were some 85 authors and editors from numerous organizations, as well as scores of technical reviewers, copyeditors, graphic artists, and photographers whose skill contributed immeasurably to the final product.

We acknowledge the extensive material and moral support given to this project by various members of the managements of all the sponsoring and supporting organizations. In many cases, organizations donated staff time and internal resources to the preparation of this book. Specifically, we would like to acknowledge John MacCallum of DoD, William Brown and Jack Walker of ERIM, and Joe Yaver of SPIE, who had the foresight and confidence to invest significant resources in the preparation of this book. We also extend our appreciation to Paul Klinefelter, Brian McCabe, and Forrest Frank of DTIC for their administrative support during the course of this program.

Supporting ERIM staff included Ivan Clemons, Jenni Cook, Tim Kellman, Lisa Lyons, Judy Steeh, Barbara Wood, and the members of their respective organizations that contributed to this project.

We acknowledge Lorretta Palagi and the publications staff at SPIE for a professional approach to the truly monumental task of transforming the manuscripts into presentable copy and the patience required to interact effectively with the authors.

We would like to pay special tribute to Nancy Hall of the IRIA Center at ERIM who administrated this at times chaotic project with considerable interpersonal skill, marshaling the numerous manuscripts and coordinating the myriad details characteristic of a work of this magnitude.

We properly dedicate this book to the people who created it and trust it will stand as a monument to their skills, experience, and dedication. It is, in the final analysis, a product of the community it is intended to serve.

Joseph S. Accetta
David L. Shumaker
Ann Arbor, Michigan

January 1993

Notices and Disclaimer

This handbook was prepared by the Infrared Information Analysis Center (IRIA) in cooperation with the International Society for Optical Engineering (SPIE). The IRIA Center, Environmental Research Institute of Michigan, is a Defense Technical Information Center-sponsored activity under contract DLA900-88-D-0392, administrated by the Defense Electronics Supply Center, Defense Logistics Agency.

This work relates to the aforementioned ERIM contract and is in part sponsored by the Department of Defense; however, the contents do not necessarily reflect the position or the policy of the Department of Defense or the United States government and no official endorsement should be inferred.

The use of product names does not in any way constitute an endorsement of the product by the authors, editors, Department of Defense or any of its agencies, the Environmental Research Institute of Michigan, or the International Society for Optical Engineering.

The information in this handbook is judged to be from the best available sources; however, the authors, editors, Department of Defense or any of its agencies, the Environmental Research Institute of Michigan, or the International Society for Optical Engineering do not assume any liability for the validity of the information contained herein or for any consequence of its use.

The Infrared and Electro-Optical Systems Handbook

Joseph S. Accetta, David L. Shumaker, *Executive Editors*

VOLUME 1. **Sources of Radiation,** George J. Zissis, *Editor*

Chapter 1. Radiation Theory, William L. Wolfe
Chapter 2. Artificial Sources, Anthony J. LaRocca
Chapter 3. Natural Sources, David Kryskowski, Gwynn H. Suits
Chapter 4. Radiometry, George J. Zissis

VOLUME 2. **Atmospheric Propagation of Radiation,** Fred G. Smith, *Editor*

Chapter 1. Atmospheric Transmission, Michael E. Thomas, Donald D. Duncan
Chapter 2. Propagation through Atmospheric Optical Turbulence, Robert R. Beland
Chapter 3. Aerodynamic Effects, Keith G. Gilbert, L. John Otten III, William C. Rose
Chapter 4. Nonlinear Propagation: Thermal Blooming, Frederick G. Gebhardt

VOLUME 3. **Electro-Optical Components,** William D. Rogatto, *Editor*

Chapter 1. Optical Materials, William L. Wolfe
Chapter 2. Optical Design, Warren J. Smith
Chapter 3. Optomechanical Scanning Applications, Techniques, and Devices, Jean Montagu, Herman DeWeerd
Chapter 4. Detectors, Devon G. Crowe, Paul R. Norton, Thomas Limperis, Joseph Mudar
Chapter 5. Readout Electronics for Infrared Sensors, John L. Vampola
Chapter 6. Thermal and Mechanical Design of Cryogenic Cooling Systems, P.Thomas Blotter, J. Clair Batty
Chapter 7. Image Display Technology and Problems with Emphasis on Airborne Systems, Lucien M. Biberman, Brian H. Tsou
Chapter 8. Photographic Film, H. Lou Gibson
Chapter 9. Reticles, Richard Legault
Chapter 10. Lasers, Hugo Weichel

VOLUME 4. **Electro-Optical Systems Design, Analysis, and Testing,** Michael C. Dudzik, *Editor*

Chapter 1. Fundamentals of Electro-Optical Imaging Systems Analysis, J. M. Lloyd
Chapter 2. Electro-Optical Imaging System Performance Prediction, James D. Howe

Chapter 3. Optomechanical System Design, Daniel Vukobratovich
Chapter 4. Infrared Imaging System Testing, Gerald C. Holst
Chapter 5. Tracking and Control Systems, Robert E. Nasburg
Chapter 6. Signature Prediction and Modeling, John A. Conant, Malcolm A. LeCompte

■ **VOLUME 5.** **Passive Electro-Optical Systems,** Stephen B. Campana, *Editor*

Chapter 1. Infrared Line Scanning Systems, William L. McCracken
Chapter 2. Forward-Looking Infrared Systems, George S. Hopper
Chapter 3. Staring-Sensor Systems, Michael J. Cantella
Chapter 4. Infrared Search and Track Systems, Joseph S. Accetta

■ **VOLUME 6.** **Active Electro-Optical Systems,** Clifton S. Fox, *Editor*

Chapter 1. Laser Radar, Gary W. Kamerman
Chapter 2. Laser Rangefinders, Robert W. Byren
Chapter 3. Millimeter-Wave Radar, Elmer L. Johansen
Chapter 4. Fiber Optic Systems, Norris E. Lewis, Michael B. Miller

■ **VOLUME 7.** **Countermeasure Systems,** David Pollock, *Editor*

Chapter 1. Warning Systems, Donald W. Wilmot, William R. Owens, Robert J. Shelton
Chapter 2. Camouflage, Suppression, and Screening Systems, David E. Schmieder, Grayson W. Walker
Chapter 3. Active Infrared Countermeasures, Charles J. Tranchita, Kazimieras Jakstas, Robert G. Palazzo, Joseph C. O'Connell
Chapter 4. Expendable Decoys, Neal Brune
Chapter 5. Optical and Sensor Protection, Michael C. Dudzik
Chapter 6. Obscuration Countermeasures, Donald W. Hoock, Jr., Robert A. Sutherland

■ **VOLUME 8.** **Emerging Systems and Technologies,** Stanley R. Robinson, *Editor*

Chapter 1. Unconventional Imaging Systems, Carl C. Aleksoff, J. Christopher Dainty, James R. Fienup, Robert Q. Fugate, Jean-Marie Mariotti, Peter Nisenson, Francois Roddier
Chapter 2. Adaptive Optics, Robert K. Tyson, Peter B. Ulrich
Chapter 3. Sensor and Data Fusion, Alan N. Steinberg
Chapter 4. Automatic Target Recognition Systems, James W. Sherman, David N. Spector, C. W. "Ron" Swonger, Lloyd G. Clark, Edmund G. Zelnio, Terry L. Jones, Martin J. Lahart
Chapter 5. Directed Energy Systems, Gary Golnik
Chapter 6. Holography, Emmett N. Leith
Chapter 7. System Design Considerations for a Visually-Coupled System, Brian H. Tsou

VOLUME I

Here c_1 is the first radiation constant and c_2 is the second radiation constant. They are given by[9] (values of the physical constants are from the same reference):

$$c_1 = 2\pi c^2 h = 3.7417749 \times 10^4 \ [\mathrm{W\ cm^{-2}\ \mu m^{-1}}] \ , \tag{1.7}$$

$$c_2 = hc/k = 1.438769 \quad [\mathrm{cm\ K}] \ , \tag{1.8}$$

where c is the speed of light *in vacuo*, h is Planck's constant, k is Boltzmann's constant, and T is the temperature in kelvins. The radiance of a blackbody is numerically $1/\pi$ times the radiant exitance. Thus, one can write

$$L_\lambda = \frac{2c^2h}{\lambda^5(e^x - 1)} \ . \tag{1.9}$$

1.2.2 Conversion to Photons

These same equations can be written in terms of photons. In this case, for monochromatic light, the equation in terms of photons is the equation in terms of energy divided by the energy of a photon, which is hc/λ:

$$L_{q\lambda} = \frac{2c}{\lambda^4(e^x - 1)} \ , \tag{1.10}$$

$$M_{q\lambda} = \frac{2\pi c}{\lambda^4(e^x - 1)} \ . \tag{1.11}$$

1.2.3 Spectral Scale Conversions

Sometimes it is useful or necessary to write the equation in terms of spectral variables other than wavelength. The conversion is carried out by the following relationship, where R is any radiometric variable and x and y are any two spectral variables:

$$R_y \, dy = R_x \, dx \ , \tag{1.12}$$

$$R_y = R_x \left(\frac{dx}{dy}\right) \ . \tag{1.13}$$

An example will illustrate. To convert from spectral radiant exitance in wavelength to wave number $\tilde{\nu}$, we perform the following calculation:

$$M_{\tilde{\nu}} = M_\lambda \left|\frac{d\lambda}{d\tilde{\nu}}\right| \ , \tag{1.14}$$

$$\lambda = 1/\tilde{\nu} \ , \tag{1.15}$$

$$\left|\frac{d\lambda}{d\bar{\nu}}\right| = \frac{1}{\bar{\nu}^2} = \lambda^2 \ , \tag{1.16}$$

$$M_{\bar{\nu}} = \frac{c_1\lambda^2}{\lambda^5(e^x - 1)} = \frac{c_1\bar{\nu}^3}{(e^x - 1)} \ . \tag{1.17}$$

1.2.4 Conversions to Other Geometries

The several forms of the blackbody relationship are radiant exitance, radiance, and energy density. To convert from radiance to radiant exitance for an isotropic radiator, such as a blackbody, multiply the radiance by π [sr]. To convert from energy density to radiant exitance *in vacuo,* multiply the energy density by $c/4$. The same relations hold true for photon and visible quantities. These are geometric relationships, fluometries. They also hold true, of course, no matter what the spectral scale. Thus, the general relationships can be written

$$M = \pi L \ , \tag{1.18}$$

$$M = cu/4 \ . \tag{1.19}$$

1.2.5 Universal Curves and Equations

Each of the different spectral distributions has a different equation. Each different temperature has a different curve. It is often useful to bring things to a common ground, to obtain, as much as possible, a universal curve or equation. For blackbody functions, there is no such thing, but some normalization can be carried out for some convenience in applications. The spectral curves can all be plotted in terms of either x or λT, the common variable. This can be seen by carrying out the spectral variable conversion from λ to x, as follows:

$$\begin{aligned} M_x &= M_\lambda \left|\frac{\partial\lambda}{\partial x}\right| \\ &= c_1\left(\frac{T}{c_2}\right)^4 \frac{x^3}{(e^x - 1)} \ . \end{aligned} \tag{1.20}$$

A plot of the function in terms of x is a single curve. The actual value must be obtained by multiplying by c_1 and the fourth power of T/c_2. The peak value occurs at about $x = 2.82$ (as shown in Table 1.5), and the value of the function at that point is 1.4214. Thus, the curve can be normalized to these values. This is one form of a "universal" curve. With such a curve, or table of values, we can calculate x based on given values for λ and T. Then we read the ratio of the value to the maximum and multiply by the maximum and the required constants to find the desired value. A program (see Sec. 1.2.9) is easier, but this is more portable. A similar situation exists for photons, but the maximum occurs at $x = 1.59$ and has a value of 0.6476. The constant is c_1 times T/c_2 to the third power. Two more similar functions for the cumulative energy flux and photon flux exist. This makes four "universal" functions.

Four more universal functions exist. They are plots of the analogs of the four above, but for the contrast functions.

1.2.6 Contrasts

The contrast may be defined as the change in the spectral radiance (or other radiometric variable) as a function of temperature. It is the temperature derivative of the function. By taking the derivative directly, it may be shown that

$$\frac{\partial R_y}{\partial T} = \frac{xe^x}{T(e^x - 1)} R_y \approx x\frac{R_y}{T} , \tag{1.21}$$

where R is any spectral radiometric function, radiance, radiant emittance, etc., and y is any spectral variable. The approximation holds for large enough values of x. These functions indicate the change in any spectral radiometric function with temperature; they are useful in the evaluation of systems that sense temperature differences. A closely related term is the relative contrast, which may be defined as

$$\frac{dR_\lambda}{R_\lambda} = \frac{xe^x}{e^x - 1}\frac{dT}{T} . \tag{1.22}$$

Once again, R is any radiometric function, e.g., $M, L, E, I,$ with respect to any spectral variable, not necessarily λ. This relationship points out that the relative change of a radiometric variable is not linearly related to the relative change in temperature. Rather it is a function of the temperature and the part of the spectrum, inherent in the variable x.

1.2.7 Maxima

The maxima of the Planck functions in the spectral domain may be found by differentiating with respect to the spectral variable, setting the result to zero, and solving the equation. The well-known result for the wavelength distribution is known as the Wien displacement law, and is written

$$\lambda_{\max} T = 2897.885 \quad [\mu\text{m K}] . \tag{1.23}$$

This is obtained from the solution described above by successive approximations to the solution given by

$$\frac{xe^x}{e^x - 1} = 5 . \tag{1.24}$$

The result is that x is 4.96511423. Therefore the Wien displacement law may be written more accurately as

$$\lambda_{\max} T = c_2 \, 4.96511423 = 2897.756 \quad [\mu\text{m K}] . \tag{1.25}$$

Table 1.5 Maxima for Different Planck Functions

Function	Spectral Variable	m	x_{max}	R_{max}
Photons	Frequency	2	1.593624260	$4.095819 \times 10^{10} T^3$
Power	Frequency	3	2.821439372	$8.989886 \times 10^{10} T^4$
Photons	Wavelength	4	3.920690395	$1.966597 \times 10^{10} T^3$
Power	Wavelength	5	4.96511423	$5.439185 \times 10^{10} T^4$
Power contrast	Wavelength	6	5.96940917	$2.062974 \times 10^{11} T^3$

The maxima are different for different functions. It may be shown that the maximum is given by the following relationship, where m represents the power of the spectral variable in the equation for radiance or radiant emittance:

$$\frac{xe^x}{e^x - 1} = |m| \ . \tag{1.26}$$

A similar treatment can be developed to obtain the expression for the maximum of the contrast functions, the temperature derivatives:

$$\frac{xe^x}{e^x - 1} = \left| \frac{x + m + 1}{2} \right| \ . \tag{1.27}$$

The values of the maxima for the different spectral distributions are displayed in Table 1.5. The entry for R_{max} is related to the maximum of the function.

1.2.8 Total Integrals

It is usually more useful to know the value of the total power emitted from a body, rather than its spectral extent. The well-known Stephan-Boltzmann law gives the total radiant exitance as

$$M = \sigma T^4 \ , \tag{1.28}$$

where σ is the Stephan-Boltzmann constant. It has been evaluated[10] and is given by

$$\sigma = \frac{2\pi^5 k^4}{15c^2h^3} = 5.67051 \times 10^{-8} \ \ [\text{W m}^{-2}\ \text{K}^{-4}] \ . \tag{1.29}$$

This expression permits the evaluation of sigma to any desired accuracy (at least to that of the fundamental constants). A similar expression can be obtained for the total output of photons:

$$M_q = \frac{2.4041(2\pi k^3 T^3)}{c^2h^3} = 1.5205 \times 10^{15} \ \ T^3 \ [\text{s}^{-1}\ \text{m}^{-2}] \ . \tag{1.30}$$

1.2.9 Computer Programs

This section provides a listing of the programs that can be used for generating the various spectral radiometric curves, the universal curves, and the integral expressions. Figure 1.1 is a plot of the expression $xe^x/(e^x - 1)$ as a function of x and therefore shows the normalized temperature contrast for different parts of the spectrum. This is the first BASIC program given at the end of this chapter. Figure 1.2 is a plot of the spectral radiant exitance [emittance] as a function of wavelength. It is generated by the second of the BASIC programs listed at the end of this chapter. They are written in QuickBasic for a VGA monitor. For other monitors the SCREEN instruction and limits on the VIEW instruction may have to be changed and some of the instructions rewritten, but it is fairly general. The program can be used for generating either a plot with the PSET instruction or a table by REMARKING the PSET instruction and unREMARKING the PRINT instruction. The spectral interval may be changed by changing the STEP value in the lambda FOR loop. The constants may be changed as the user desires. All the LOCATE instructions will have to be changed if the user desires a different set of temperatures for the program. Figure 1.3 is a plot of spectral radiant exitance [emittance] as a function of wave number. The only part of the program that is different is the settings of the WINDOW values and the FOR loop that calculated the values. The values of this spectral radiant exitance [emittance] are much smaller than those for the wavelength because the spectral interval is much smaller. Figure 1.4 is a logarithmic plot of the spectral radiant emittance [exitance] as a function of

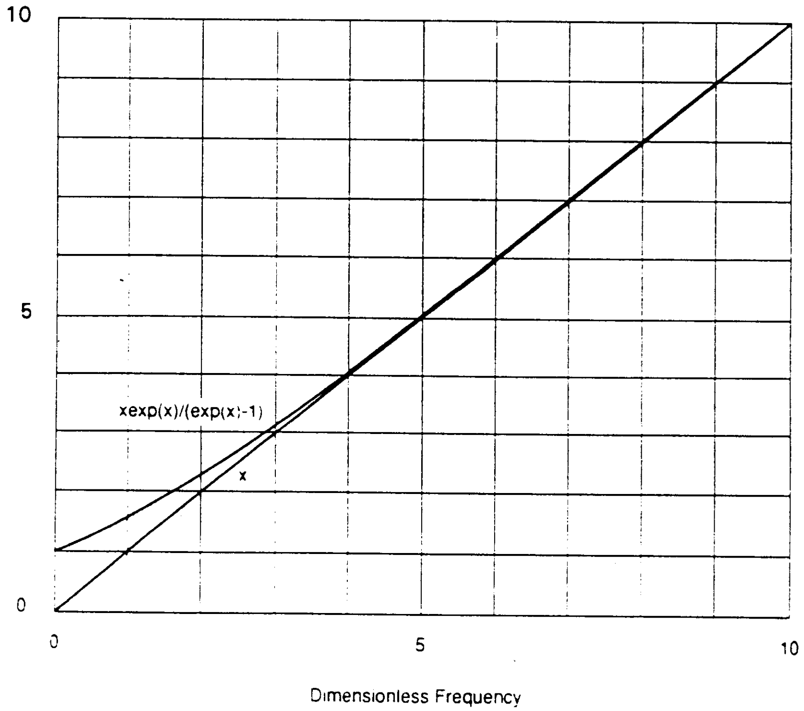

Fig. 1.1 The expression $x\exp(x)$ [$\exp(x) - 1$] versus x.

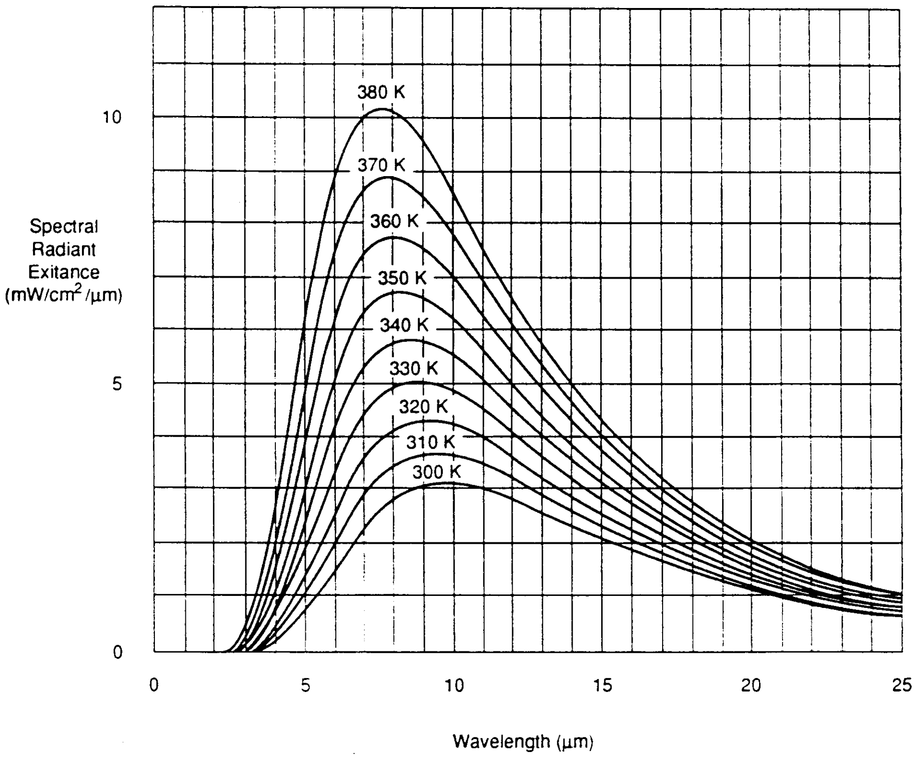

Fig. 1.2 Spectral radiant exitance versus wavelength.

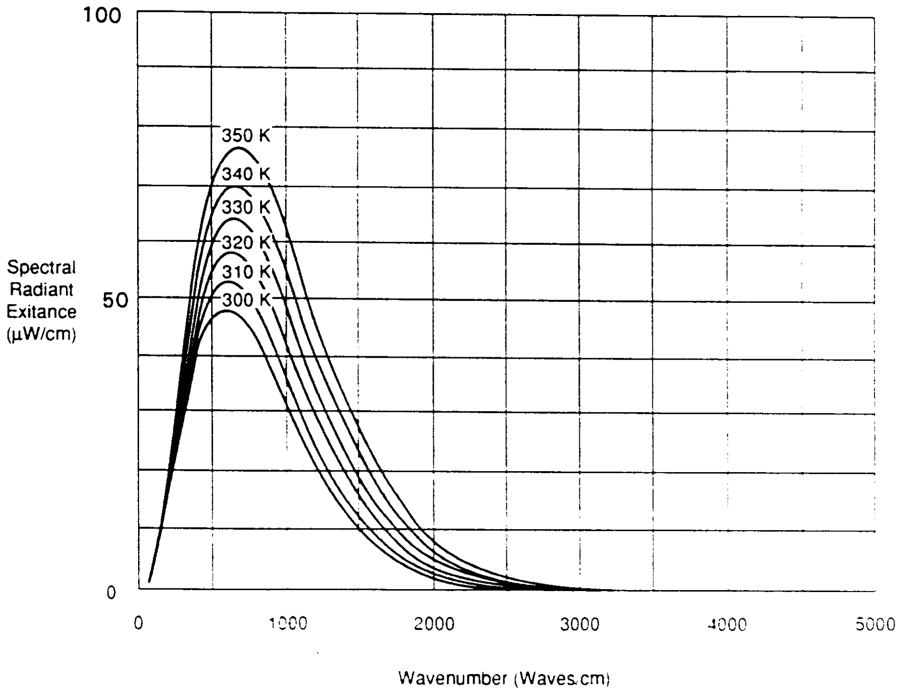

Fig. 1.3 Spectral radiant exitance versus wave number.

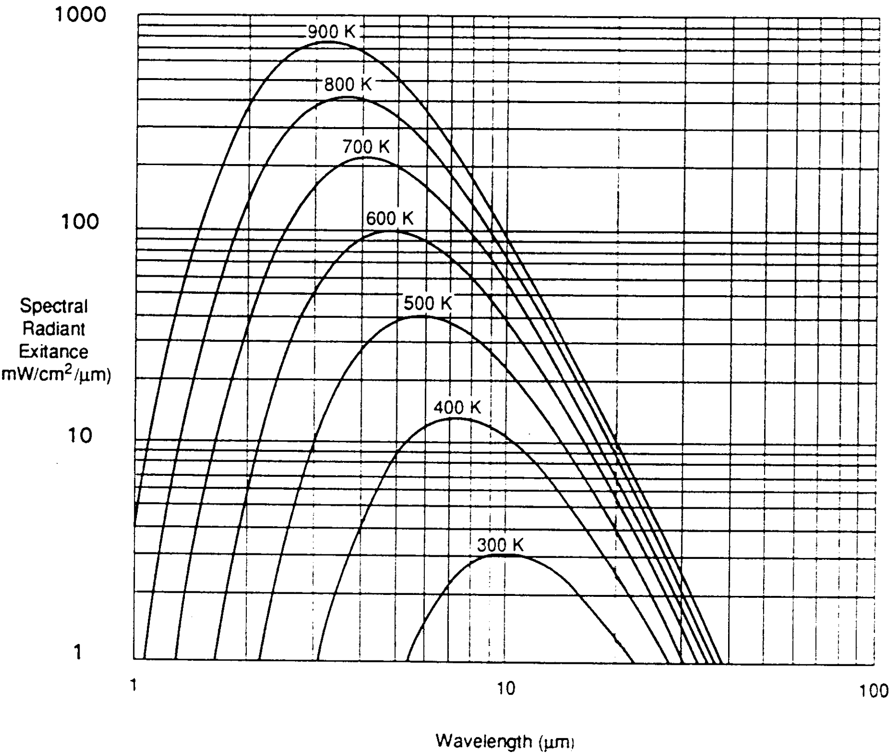

Fig. 1.4 Spectral radiant exitance versus wavelength.

the wavelength. It illustrates the fact that the curves are all the same shape in this scale. They merely slide along the line that represents the Wien displacement law, which in this scale is a straight line. Figure 1.5 is a similar curve for the spectral radiant exitance [emittance] on a wave number basis.

The next two curves are so-called universal ones. Figure 1.6 is a plot of the spectral radiant exitance [emittance] as a function of x, and normalized to its maximum value of 1.4214 at its (dimensionless) frequency of 2.8214, as given in Table 1.5. To obtain a value for a particular wavelength or wave number and temperature, calculate x; find the fractional value from this curve or table at that x; then multiply by 1.4214 and the appropriate version of the constant, such as $c_1(T/c_2)^4$ for the wavelength distribution. Figure 1.7 is a similar curve for the photon distribution. Figures 1.8 and 1.9 are the cumulative curves for the energy and photon distributions, respectively. They have both been generated using the series calculation for the integral. This approximation arises as follows. The Planck function can be written in terms of the dimensionless frequency x as follows:

$$M_x = c_1\left(\frac{T}{c_2}\right)^4 \frac{x^3}{e^x - 1} . \tag{1.31}$$

The integral may then be written as

$$M_{0-x} = \frac{c_1}{c_2^4} T^4 \int_0^x \frac{x^3}{e^x - 1}\, dx . \tag{1.32}$$

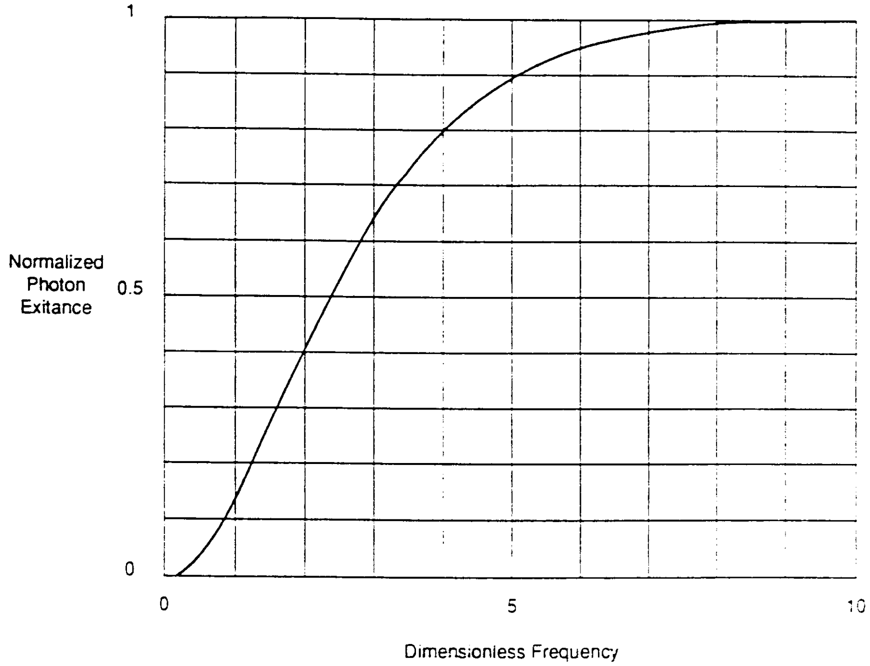

Fig. 1.9 Normalized photon exitance versus dimensionless frequency.

The integrand may be represented as an infinite geometric series:

$$\frac{x^3}{e^x - 1} = x^3 \sum_{m=1}^{\infty} e^{-mx} \; . \tag{1.33}$$

Then the integral may be integrated successively by parts to yield the result:

$$\int_0^{x_1} \frac{x^3}{e^x - 1}\, dx = \sum_{m=1}^{\infty} [(mx)^3 + 3(mx)^2 - 6(mx) + 6] e^{-mx} m^{-4} \; . \tag{1.34}$$

The integral in any spectral band can then be found by integrating from 0 to x_1 and from 0 to x_2 and subtracting. Other forms are found the same way. Any integral applies for any spectral function, but they are different for energy, photons, energy contrast, and photon contrast. They are

$$M_{q0-x} = 2\pi c \frac{T^3}{c_2^3} \sum_{m=0}^{\infty} [(mx)^2 + 2mx + 2] e^{-mx} m^{-3} \; , \tag{1.35}$$

$$\begin{aligned} \frac{\partial M_{0-x}}{\partial T} = \frac{c_1 T^3}{c_2^4} \sum_{m=0}^{\infty} [(mx)^4 + 4(mx)^3 - 12(mx)^2 \\ + 24mx + 24] e^{-mx} m^{-4} \; . \end{aligned} \tag{1.36}$$

$$\frac{\partial M_{q0-x}}{\partial T} = \frac{2\pi c T^2}{c_2^3} \sum_{m=0}^{\infty} [(mx)^3 + 3(mx)^2 - 6mx + 6] e^{-mx} m^{-3} \; . \tag{1.37}$$

about 600 nm, is assumed. In the more general case, both the value and the wavelength must be known and cited. Based on the Planck equation, the "brightness" temperature is given implicitly by

$$\frac{c_1}{\lambda^5[\exp(c_2/\lambda T_b) - 1]} = \frac{\varepsilon(\lambda)c_1}{\lambda^5[\exp(c_2/\lambda T) - 1]} \ . \qquad (1.63)$$

Because the constants and the wavelengths are identical for the blackbody and the real body,

$$\exp(c_2/\lambda T_b) - 1 = \varepsilon^{-1}[\exp(c_2/\lambda T) - 1] \ . \qquad (1.64)$$

This can be solved explicitly for T_b, but not much is added to the understanding. It is

$$T_b = \frac{\lambda}{c_2} \ln\{1 + \varepsilon^{-1}[\exp(c_2/\lambda T) - 1]\} \ . \qquad (1.65)$$

In the region for which the exponential is much greater than one, the expression simplifies to

$$T_b = c_2(\lambda \ln\varepsilon + c_2)^{-1} \ . \qquad (1.66)$$

1.5.3 Distribution Temperature

Distribution temperature[27] is defined as the temperature of a blackbody that best matches the spectral distribution of the real body. A subcategory is the ratio temperature, which requires only that the match be made at two spectral points, for example, wavelengths. For this ratio temperature, the equality of the radiant exitances [emittances] dictates

$$\varepsilon_1\lambda_1^{-5}[\exp(c_2/\lambda_1 T) - 1]^{-1} = \varepsilon_2\lambda_2^{-5}[\exp(c_2/\lambda_2 T) - 1]^{-1} \ . \qquad (1.67)$$

For the Wien approximation, the expression reduces to

$$T_d = \frac{\dfrac{c_2(\lambda_2 - \lambda_1)}{\lambda_2\lambda_1}}{\ln\left[\dfrac{M_1}{M_2}\dfrac{\varepsilon_1}{\varepsilon_2}\left(\dfrac{\lambda_1}{\lambda_2}\right)^5\right]} \ . \qquad (1.68)$$

This may also be written with the reduced wavelength as

$$T_d = \frac{c_2}{\lambda} \frac{1}{\ln\left[\dfrac{M_1}{M_2}\dfrac{\varepsilon_1}{\varepsilon_2}\left(\dfrac{\lambda_1}{\lambda_2}\right)^5\right]} \ , \qquad (1.69)$$

where

$$\frac{1}{\lambda} = \frac{1}{\lambda_1} - \frac{1}{\lambda_2} \ . \qquad (1.70)$$

```
'draw the grid lines
FOR x = xmin TO xmax STEP 1                 'vertical lines
  LINE (x, ymin)-(x, ymax), 8               'the 8 gives gray grid lines
NEXT x
FOR y = ymin TO 1.1 * ymax STEP .001        'horizontal lines
  LINE (xmin, y)-(xmax, y), 8               '1.1x to get top line
NEXT y

'calculate the curve for different values of T and lambda
FOR T = 300 TO 380 STEP 10
  FOR lambda = 1 TO 25 STEP .01
    x = c2 / lambda / T                     'the expression for x
    M = c1 / lambda ^ 5 / (EXP(x) - 1)      'Planck's equation
    'PRINT lambda, M                        'option for printing
    PSET (lambda, M), 12                    'plotting the values;
  NEXT lambda
NEXT T                                                 'the 12 gives a red line

'Calculate the Wien displacement law
FOR T = 100 TO 400 STEP .1
    lambdax = 2898.8 / T
    x = c2 / lambdax / T                    'the expression for x
    M = c1 / lambdax ^ 5 / (EXP(x) - 1)     'Planck's equation
    'PRINT lambda, M                        'option for printing
    PSET (lambdax, M), 14                   'plotting the values
NEXT T



'Radiant exitance vs wavenumber
CLS
SCREEN 9                                    'set the screen for EGA
VIEW (100, 60)-(600, 275)                   'set an screen area
xmin = 0: xmax = 5000                       'set extreme ordinate values
ymin = 0: ymax = .0001                      'set extreme abscissa values
WINDOW (xmin, ymin)-(xmax, ymax)            'set appropriate calculational values

'set up constants
c = 2.9975E+10
h = 6.626E-34
pi = 3.14159
c2 = 14399
c1 = 2 * pi * c * c * h                     'c1 in units of W/cm2
                                            'per reciprocal cm
'locate titles and axis values appropriately
LOCATE 23, 15: PRINT "Figure 3. Spectral radiant exitance vs wavenumber"
LOCATE 22, 35: PRINT "Wavenumber [waves/cm]"
LOCATE 8, 1: PRINT "Spectral"
LOCATE 9, 1: PRINT "Radiant"
LOCATE 10, 1: PRINT "Exitance"
LOCATE 11, 1: PRINT "[uW/cm]"
LOCATE 20, 10: PRINT 0
LOCATE 5, 9: PRINT 100
LOCATE 12, 10: PRINT 50



LOCATE 21, 12: PRINT 0
LOCATE 21, 23: PRINT 1000
LOCATE 21, 35: PRINT 2000
LOCATE 21, 48: PRINT 3000
LOCATE 21, 61: PRINT 4000
LOCATE 21, 73: PRINT 5000

'draw the grid lines
FOR x = xmin TO xmax STEP 500               'vertical lines
  LINE (x, ymin)-(x, ymax), 8               'the 8 gives gray lines
NEXT x
FOR y = ymin TO 1.1 * ymax STEP .00001      'horizontal lines
  LINE (xmin, y)-(xmax, y), 8
NEXT y

'calculate the curve for different values of T and nu
FOR T = 300 TO 350 STEP 10
  FOR nu = 40 TO 5000 STEP 10
    x = c2 * nu / 10000 / T                 'the expression for x
    M = c1 * nu ^ 3 / (EXP(x) - 1)          'Planck's equation
    'PRINT nu, M                            'option for printing
    PSET (nu, M), 12                        'plotting the values
  NEXT nu
NEXT T
```

References

1. "The International System of Units (SI)," Special Publication 330, The National Bureau of Standards (now The National Institute of Standards and Technology), U.S. Department of Commerce (1972).
2. ANSI Standard Z7.1-1967(RP-16), American National Standards Institute (1967).
3. R. C. Jones, "Terminology in photometry and radiometry," *Journal of the Optical Society of America* **53,** 1314 (1963).
4. F. E. Nicodemus in a discussion column of I. Spiro, *Optical Engineering* **13,** G165 and G173 (1974).
5. J. Geist and E. Zalewski, "Chinese restaurant nomenclature for radiometry," *Applied Optics* **12,** 435 (1973).
6. K. D. Mielenz, "International comparison of photometric base units," *Journal of Research of the NBS* **92,** 335 (1987).
7. *CIE Proceedings* **6,** 67 (1924); see also J. W. T. Walsh, *Photometry,* Dover (1965).
8. M. Planck, *Theory of Heat,* Macmillan, New York (1957).
9. E. R. Cohen and B. N. Taylor, "The 1986 adjustment of the fundamental physical constants," Codata Bulletin 63, Pergamon Press, Elmsford, NY (1986).
10. M. A. Bramson, *Infrared, A Handbook for Applications,* Plenum Press, New York (1966).
11. R. B. Johnson and E. E. Branstetter, "Integration of Planck's equation by the Laguerre-Gauss quadrature method," *Journal of the Optical Society of America* **64,** 1445 (1974).
12. J. C. Richmond, "Rationale for emittance and reflectivity," *Applied Optics* **21,** 1 (1982).
13. W. L. Wolfe, "Proclivity for emissivity," *Applied Optics* **21,** 1 (1982).
14. F. E. Nicodemus, J. C. Richmond, J. J. Jsia, I. W. Ginsberg, and T. Limperis, "Geometrical considerations and nomenclature in reflectance," National Bureau of Standards, U.S. Department of Commerce (1977).
15. M. Born and E. Wolfe, *Electromagnetic Theory of Optics,* Pergamon Press, New York (1959).
16. F. E. Nicodemus, "Directional reflectance and emissivity of an opaque surface," *Applied Optics* **4,** 767 (1965).
17. G. Kirchhoff, "On the relation between the radiating and absorbing powers of different bodies for light and heat," *Philosophical Magazine and Journal of Science* **20** (Fourth Series), 130 (1860).
18. H. O. McMahon, "Thermal radiation from partially transparent bodies," *Journal of the Optical Society of America* **40,** 376 (1950).
19. F. E. Nicodemus, "Radiance," *American Journal of Physics* **31,** 368 (1963).
20. W. J. Smith, *Modern Optical Engineering,* 2nd ed., McGraw-Hill, New York (1990); see also J. Rainwater, "Generalization of the Abbe sine law in geometric optics," *American Journal of Physics* **32,** 626–631 (1964).
21. S. Liebes, Jr., "On the ray invariance of B/n^2," *American Journal of Physics* **37,** 932 (1969); see also A. Arkangy, "Liouville's theorem and the intensity of beams," *American Journal of Physics* **25,** 519 (1957).
22. H. C. Hottel and A. F. Sarofim, *Radiative Transfer,* McGraw-Hill, New York (1967).
23. P. Moon, *The Scientific Basis of Illuminating Engineering,* McGraw-Hill, New York (1936).
24. D. C. Hamilton and W. R. Morgan, National Advisory Committee on Aeronautics Technical Note 2836 (1952).
25. R. W. Boyd, *Radiometry and the Detection of Radiation,* John Wiley & Sons, New York (1983).
26. W. L. Wolfe, "Photometry and radiometry," in *Physical Optics and Light Measurements,* D. Malacara, Ed., Academic Press, New York (1980).
27. W. L. Wolfe, "Radiometry," in *Applied Optics and Optical Engineering,* R. R. Shannon, J. C. Wyant, Eds., Academic Press, New York (1980).
28. Committee on Colorimetry, *The Science of Color,* Thomas Y. Crowell (1963).
29. H. E. White, *Introduction to Atomic Spectra,* McGraw-Hill, New York (1934).
30. Herzberg, G., *Spectra of Diatomic Molecules,* Van Nostrand, New York (1950).
31. Adapted from E. J. McCartney, *Absorption and Emission by Atmospheric Gases,* John Wiley & Sons, New York (1983).
32. Adapted from M. Garbuny, *Optical Physics,* Academic Press, New York (1965).

that denotes the center wavelength used. The subscripts U, pg, B, V, and R denote, respectively, the ultraviolet, photographic, blue, yellow or visual, and red bands, and have center wavelengths given by[15]

$$
\begin{aligned}
m_U &= U = 3650\ \text{Å} \\
m_{pg} &= \ 4400\ \text{Å} \\
m_B &= B = 4350\ \text{Å} \\
m_V &= V = 5500\ \text{Å} \\
m_R &= \ 7000\ \text{Å}\ .
\end{aligned}
$$

The effective wavelengths, effective bandwidths, and flux for a zero magnitude star within the respective band pass is given[15,18] in Table 3.7.

A body that has a visual magnitude of $m_V = +1$ and $m_V = 0$ gives an exoatmospheric illuminance normal to the rays of 1.05×10^{-10} lm cm^{-2} and 2.65×10^{-10} lm cm^{-2} respectively.

The absolute magnitude M is defined as the apparent magnitude a star would have at a distance of 10 parsecs (pc = 202,625 AU = 3.09×10^{18} cm). With R as the interstellar distance in kiloparsecs (kpc) and $A(R)$ the interstellar extinction in magnitudes to the star, the absolute and apparent magnitudes are related by

$$M = m - 10 - 5 \log_{10} R - A(R)\ . \tag{3.23}$$

Table 3.7 Definition of Zero Magnitude Spectral Flux Density as a Function of Wavelength (from Ref. 15)

Band	λ_c (μm)	$\Delta\lambda_c$ (μm)	Flux (m_λ=0) W cm^{-2}μm^{-1}
U	0.365	0.068	4.27×10^{-12}
B	0.44	0.098	6.61×10^{-12}
V	0.55	0.089	3.72×10^{-12}
R	0.70	0.72	1.74×10^{-12}
I	0.88	0.24	8.32×10^{-13}
J	1.25	0.38	3.31×10^{-13}
H	1.65	0.30	1.28×10^{-13}
K	2.22	0.48	4.14×10^{-14}
L	3.6	0.70	6.38×10^{-15}
M	5.0	1.73	1.82×10^{-15}
N	10.6	4.33	8.7×10^{-17}
Q	21	5.8	6.5×10^{-18}

VOLUME 2

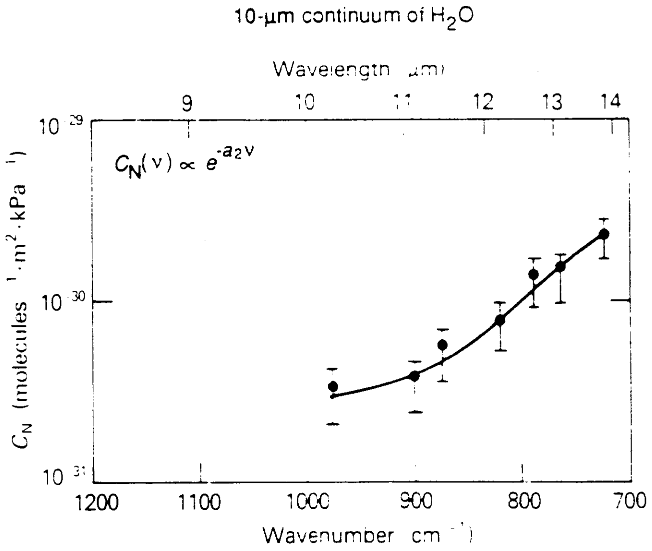

Fig. 1.18 Nitrogen-broadening coefficient as a function of wave number from 700 to 1200 cm^{-1} at 296 K.

Based on the data presented and Birnbaum's line-shape formula, a simple formula for the nitrogen-broadened water-vapor-continuum absorption coefficient from 700 to 1100 cm^{-1} and for typical atmospheric temperatures is given by[73]

$$\beta_{\text{cont}} = 7.4 \times 10^5 \exp(-0.00839\nu)\left\{\left(\frac{T_0}{T}\right)^3 p_{N_2} - 17.96 \exp\left[(0.00374\nu - 1680\left(\frac{1}{T} - \frac{1}{T_0}\right)\right] p_{H_2O}\right\}\frac{p_{H_2O}}{T} \ (\text{km}^{-1}) \ . \qquad (1.125)$$

where p is in atm, ν is in wave numbers, and $T_0 = 296$ K.

An excellent review of experimental measurements in the 10-μm region by Grant[55] makes the following additional points:

1. Oxygen does not broaden as effectively as nitrogen and must be included in a realistic model of the earth's atmosphere. A broadening coefficient of $F = 0.75 \pm 0.1$ for oxygen relative to nitrogen was measured by Nordstrom et al.[74] Using Eq. (1.118), this means air has an effective broadening of 0.95.
2. Understanding the local-line structure is critical in determining the true continuum. Line positions are known reasonably well; however, line strength and half-width are not known with enough accuracy.

Long-path field measurements by Devir et al.[75] are in excellent agreement with the laboratory measurements of Burch and Alt[66] and Peterson et al.[67] in this window region concerning the water-vapor continuum. The measured

Table 1.22 **Oscillator Parameters for Atmospheric Refractivity**

Mode Number	ν_i (cm^{-1})	$\Delta\varepsilon_i$^{a}
1	∞	$4.744 \times 10^{-4} P_{dry}/T$
2	114,000.0	$1.053 \times 10^{-3} P_{dry}/T$
3	62,400.0	$2.338 \times 10^{-5} P_{dry}/T$
4	111,575.0	$1.303 \times 10^{-3} P_{H_2O}/T$
5	3740.0	$1.48 \times 10^{-5} P_{H_2O}/T$
6	1595.0	$1.158 \times 10^{-4} P_{H_2O}/T$
7	125.0	$7.488 P_{H_2O}/T^2$

[a] P_{dry} and P_{H_2O} are in units of kPa; T is in units of kelvin.

water vapor. Temperature and pressure dependence of the band strength are determined by the gas number density. The exception is the rotational band, for which, because of the low-band-center frequency, the population difference factor in Eq. (1.82) contributes another factor of $1/T$ to the band strength. This Sellmeier model reproduces available experimental data at visible and microwave frequencies[143,144] and allows reasonable predictions (± 0.5 N units) at infrared frequencies for a humid atmosphere. More accurate approaches are possible but will be more complicated.[139] A small discrepancy also exists between $N_{dry}(\nu = 0)$ and N_{rf}, which can be explained by the neglected contributions of the 60 GHz O_2 band and other minor contributions from CO_2, N_2O, and CH_4 infrared absorption bands.

1.3.5.2 Earth-Atmosphere Geometry

Given that the index of refraction depends on density and the density of the atmosphere depends on altitude (see Sec. 1.2.4), then light propagating in the atmosphere will be bent (typically toward lower altitudes or regions of higher density). To account for this geometrically, a suitable coordinate system must be used such as that illustrated in Fig. 1.44.[145] An observer at altitude s (in units of feet) can see beyond the geometrical horizon. A formula for calculating the optical horizon oh (in units of nautical miles) in a standard atmosphere is given by

$$oh = 1.14 s^{1/2} \; . \tag{1.178}$$

The accuracy of Eq. (1.178) depends on deviations of atmospheric density from standards that are almost always present. This point is discussed further in the next two sections. The angle between OH″ and OH is the refraction correction angle and is listed in Table 1.23 for altitudes near sea level. It is interesting to note that the angular extent of the sun is 32 arc min and the maximum refraction correction is 34.5 arc min; thus, even though the setting sun is below the geometrical horizon it can still be observed. Note also from

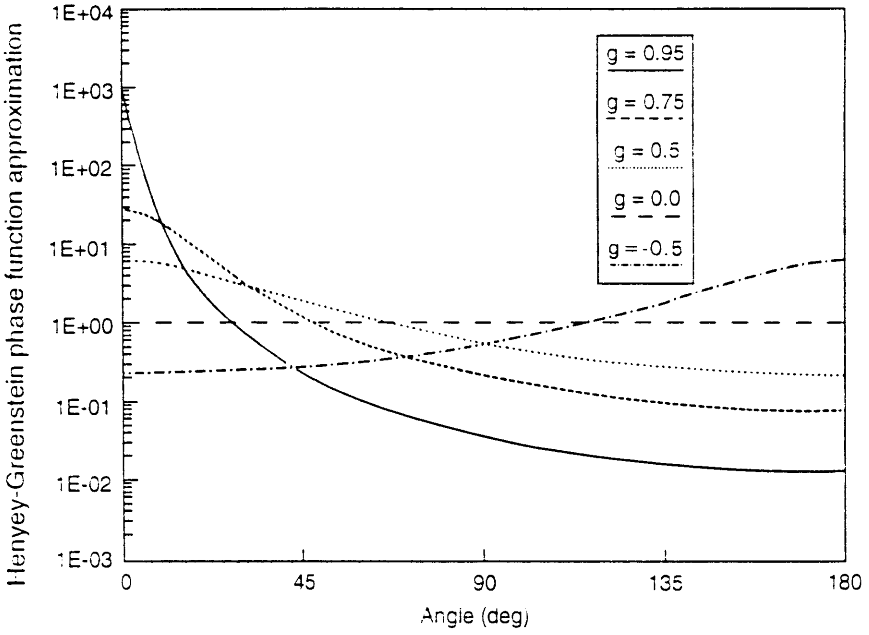

Fig. 1.60 Example Henyey-Greenstein phase function.

$$P(\cos\theta) = \frac{1 - g^2}{(1 - g^2 - 2g\cos\theta)^{3/2}} . \qquad (1.274)$$

For this phase-function approximation, the expansion coefficients as in Eq. (1.272) are given by $\omega_n = (2n - 1)g^n$. For an asymmetry parameter of -1 (-1), the phase function is completely in the forward (backward) direction. For $g = 0$, the scatter is isotropic. Example Henyey-Greenstein phase functions are shown in Fig. 1.60.

1.4.4.3 Temporal Effects—Pulse Stretching

So far, we have considered only steady-state conditions, ignoring the fact that in the process of scattering from particulate media, the "time of flight" of the individual photons is increased. This effect is of importance, for example, when the source of radiation, e.g., a laser, is being temporally modulated. An analysis of this effect is usually accomplished through the use of Monte Carlo techniques, e.g., see Bucher.[188] There are, however, analytic formulas for this effect. One, due to Stotts,[189] is the following:

$$\Delta t = \frac{z}{c}\left\{\frac{0.30}{a\tau\theta_{rms}^2}\left[(1 - 2.25a\tau\theta_{rms}^2)^{1.5} - 1\right] - 1\right\} . \qquad (1.275)$$

where z is the propagation distance in medium, c is the propagation velocity in medium, θ_{rms} is the rms scatter angle, a is the single-scatter albedo, and $\tau = \beta_{sca}z$.

VOLUME 4

Table 3.6 Schwesinger Equation Constants

Support	a_0	a_1	a_2
One point at 0 deg	0.06654	0.7894	0.4825
Two points at 45 deg	0.05466	0.2786	0.1100
Two points at 60 deg	0.09342	0.7992	0.6875
180 deg sling	0.00074	0.1067	0.0308

Astigmatism is induced in the mirror optical surface if the two support points are not placed in the same plane as the mirror's center of gravity. For minimum radial self-weight deflection, one of the best supports is a simple sling or band wrapped around the lower 180 deg of the mirror.[41]

3.6.2 Lightweight Mirrors

Conventional solid-glass right circular cylinder mirrors are relatively heavy, with a weight given by[42]:

$$W = 246D^{2.92} , \tag{3.71}$$

where W is the mirror weight in kilograms and D is the mirror diameter in meters. For many applications, such as satellite systems, a mirror with a weight given by Eq. (3.71) is unacceptably heavy. Pointing and tracking systems are often relatively limited in drive torque, requiring the use of low moment of inertia and, hence, lightweight mirrors. The thermal inertia of solid mirrors may be excessive, requiring a lightweight mirror design. Lightweight mirrors are usually much more expensive to fabricate than conventional solid mirrors and are difficult to mount.

Conventional lightweight mirrors have about 30 to 40% of the weight of the same diameter solid six-to-one aspect ratio mirror. The weight of these mirrors is estimated by[42]:

$$W = 120D^{2.82} , \tag{3.72}$$

where W is the mirror weight in kilograms and D is the mirror diameter in meters.

State-of-the-art lightweight mirrors have about 20% of the weight of the same diameter solid six-to-one aspect ratio mirror. The weight of these mirrors is estimated by[42]:

$$W = 53D^{2.67} , \tag{3.73}$$

where W is the mirror weight in kilograms and D is the mirror diameter in meters. Figure 3.14 compares mirror weight as a function of diameter for lightweight and solid mirrors.

A useful parameter in evaluating performance of a lightweight mirror is the ratio of the self-weight deflection of the lightweight mirror to the self-weight deflection of a solid mirror of the same diameter. If this ratio exceeds

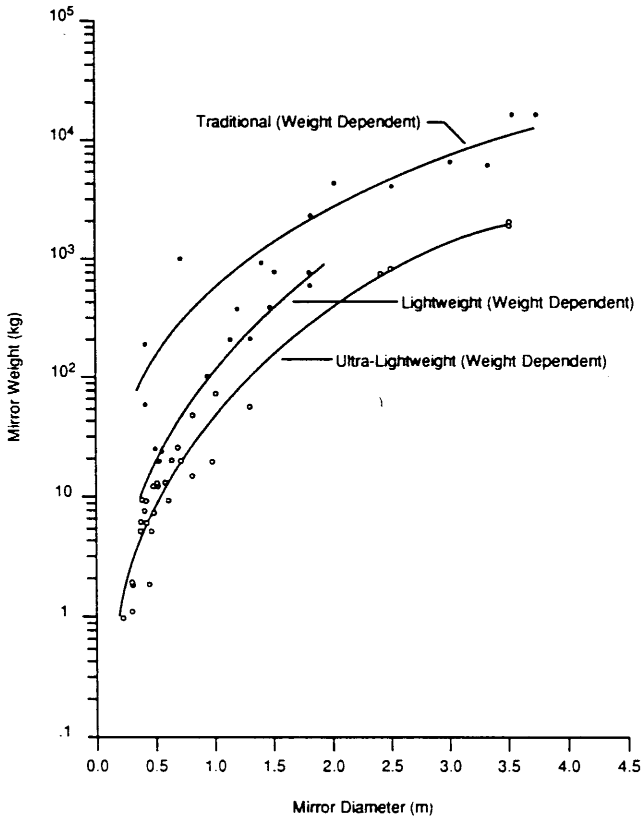

Fig. 3.14 Mirror weight as a function of diameter for traditional, lightweight, and ultra-lightweight mirrors (from Ref. 42).

unity, the lightweight mirror has less stiffness than the conventional solid mirror. A lightweight mirror that is not as stiff as a solid mirror of the same weight has very limited utility. More common, but less useful performance parameters for lightweight mirrors are the area density, and also weight in terms of percentage of an equivalent diameter six-to-one aspect ratio solid.[43]

Contoured Back Mirrors. Contouring the back of a lightweight mirror reduces the weight and improves the stiffness-to-weight ratio of the mirror. Three types of mirror back contour are used: the single arch, the double arch, and the symmetric shape. A contoured back mirror of optimum design can have a deflection ratio of 0.50 or less when compared to a solid mirror of the same weight.[44]

The simplest type of contoured back mirror is produced by tapering the back of the mirror from a thick hub to a thin edge. A straight taper is easiest to produce. Self-weight deflection for a single-tapered mirror is obtained by a parabolic taper on the back of the mirror, with the vertex of the parabola coincident with the back of the mirror. If a parabolic taper is used, this type of contoured back mirror is called a *single-arch mirror*. Deflection efficiency of the single arch is poor, with a deflection ratio of about 2 when compared with a solid mirror of the same weight. Weight of a single-arch mirror can be

$$h_B^3 = (2h_F + h_c)^3 - \left(1 - \frac{\eta}{2}\right) h_c^3 \ , \tag{3.78}$$

$$D = \frac{E h_B^2}{12(1 - \nu^2)} \ , \tag{3.79}$$

where h_F is the face plate thickness (the backplate is assumed to have the same thickness) and h_B is the equivalent thickness of the mirror.

The weight of a sandwich mirror is given by:

$$W = \frac{\pi}{4} \rho d^2 (2h_F + \eta h_c) \ . \tag{3.80}$$

There is an optimum relationship between faceplate thickness, rib thickness, and cell size for minimum self-weight deflection. Figures 3.16 and 3.17 relate these parameters for an open-back mirror and a sandwich mirror, respectively. Some caution is indicated in employing these figures, due to a fabrication issue involving mirror surface deformation corresponding to the structure of the ribs. During fabrication, the mirror faceplate will deflect between ribs due to polishing pressure. This deflection, called *quilting* (because the periodic pattern of deflection resembles the square of a quilt), is permanently polished into the mirror surface figure. Quilting causes a reduction in energy in the central maximum of the diffraction disk. Reduction of quilting is possible by increasing the faceplate thickness, decreasing the spacing between ribs, or by using lighter polishing pressures. Figure 3.18 gives the representative quilting for different types of cells.

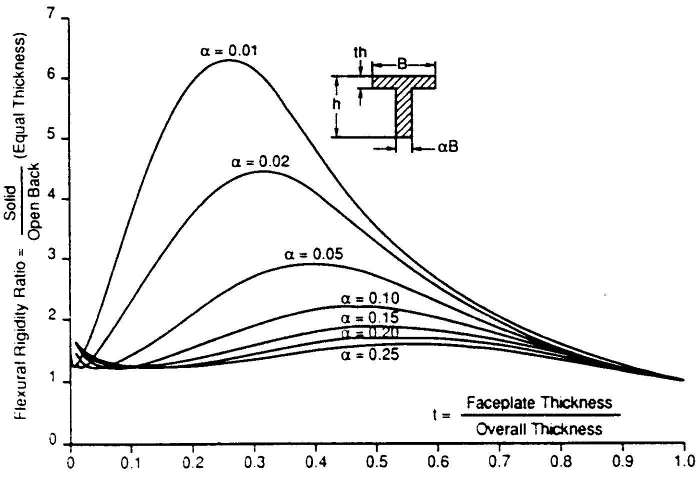

Fig. 3.16 Open back mirror flexural rigidity (from Ref. 43).

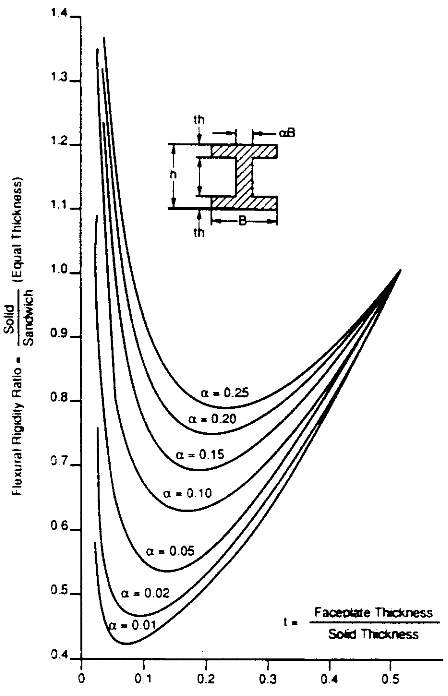

Fig. 3.17 Sandwich mirror flexural rigidity (from Ref. 43).

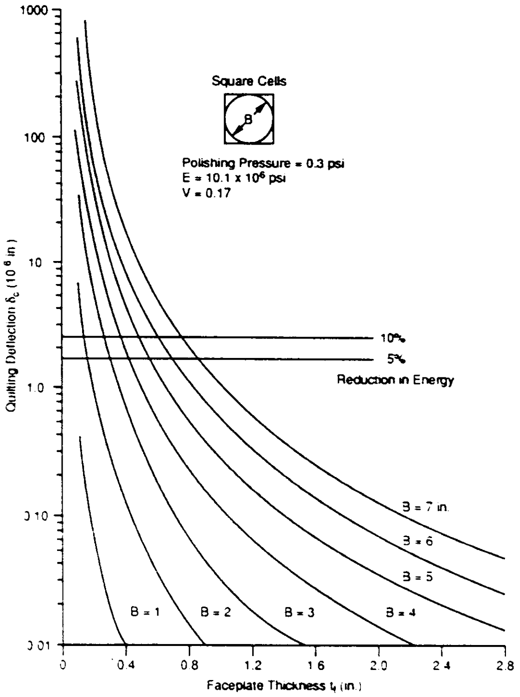

Fig. 3.18 Faceplate quilting under polishing pressure for lightweight mirrors (from Ref. 43).

applications, this tolerance is too extreme and can be relaxed. A more realistic tolerance for flatness and tilts of the contact surface is a tolerance equivalent to the surface deformation in the contact area.

An alternative to very small tolerances in the contact areas is to allow one contact in each pair of contacts to rotate with respect to the other. The simplest arrangement for providing this rotation is a spherical surface in contact with a cone. This sphere and cone geometry is easily modified to that of a sphere sliding in a cylinder. Three such sphere cylinder contacts around the edge of a mirror provide a semikinematic mount that is also athermalized. A change in physical size of the mount with temperature due to a difference in thermal coefficient of expansion between mount and optic is removed by radial translation of the spheres in their respective cylindrical mounts. This type of mirror mount has been patented by Mesco[62] and is shown in Fig. 3.20.

Flexural Mirror Mounts. Flexural mirror mounts are similar in principle to semikinematic mounts.[63] Kinematic principles are used to determine the stiffness of each flexure used to mount the mirror. The classic flexural mirror mount uses three flexures attached to the edge of the mirror. Each flexure is stiff in the axial and tangential directions and is compliant in the radial direction. This combination of stiffness and compliance accurately locates the mirror, yet allows the mount to expand or contract radially with respect to the mirror. The mirror is isolated from stresses due to temperature changes and thermal coefficient of expansion difference between mirror and mount.[64]

The stiffness of a flexure-mounted mirror is given by[63]:

$$K_R = \frac{3}{2}(K_{FR} + K_{FT}) \ , \tag{3.100}$$

$$K_A = 3K_{FA} \ , \tag{3.101}$$

where

K_R = radial stiffness of the mirror mount
K_{FR} = radial stiffness of one mirror mount flexure
K_{FT} = tangential stiffness of one mirror mount flexure
K_A = axial stiffness of the mirror mount
K_{FA} = axial stiffness of one mirror mount flexure.

Error in locating the flexures can induce bending forces into the mirror. This lack of assembly accuracy complicates the design of the mirror mount flexures. The effect of assembly inaccuracy is reduced by introducing additional directions of stiffness and compliance into each mirror mount flexure. In the classic three-flexure design, assembly inaccuracy effects are reduced by placing a set of flexures between the mounting flexures and the mirror. This additional set of flexures provides compliance in rotation about two orthogonal axes. Both rotation axes are parallel to the plane of the mirror surface. Further reduction in mirror surface deflection is possible by attaching the flexures to the mirror in the plane of the center of gravity.[65] An example of a flexure-mounted mirror is shown in Fig. 3.21.

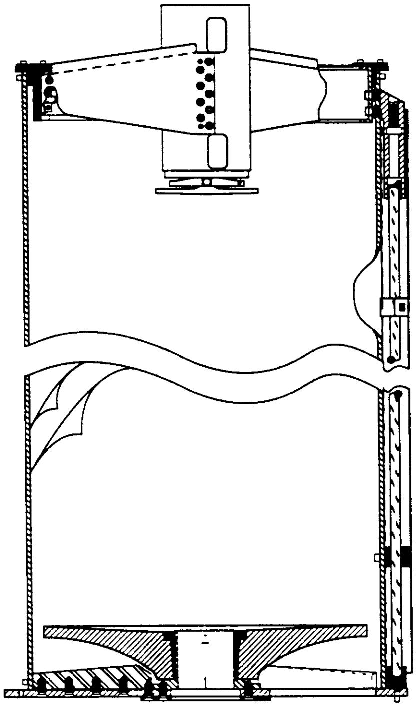

Fig. 3.24 Metering rods maintain focus in an athermalized Cassegrain telescope (courtesy of RMR Design Group, Inc., Tucson, Arizona).

disadvantage of the graphite epoxy composite materials is dimensional instability caused by the absorption of water. A change in humidity can cause a graphite epoxy structure to change in size enough to affect the performance of the optical system.[73] Humidity absorption in graphite epoxy structures is reduced by cladding the structure with a flexible hermetically sealed membrane. Damage to the membrane in service and residual water inside the membrane are two problems of this approach.

3.8 EXAMPLE PROBLEMS

3.8.1 Window Design

A 500-mm-diam circular ZnSe window is used on an aircraft flying at an altitude of 12 km. Instrument bay pressure and temperature are 27 KPa and 300 K, respectively. Ambient conditions are a pressure of 19 KPa and a temperature of 217 K. A window failure probability of 10^{-4} with a safety factor of 4 is acceptable. Calculate the safe window thickness and the deflections due to pressure and temperature differentials.

Solution. Failure strength is given using Weibull statistics. Solving Eq. (3.19) for stress, and using the lowest values for ZnSe in Table 3.7:

VOLUME 5

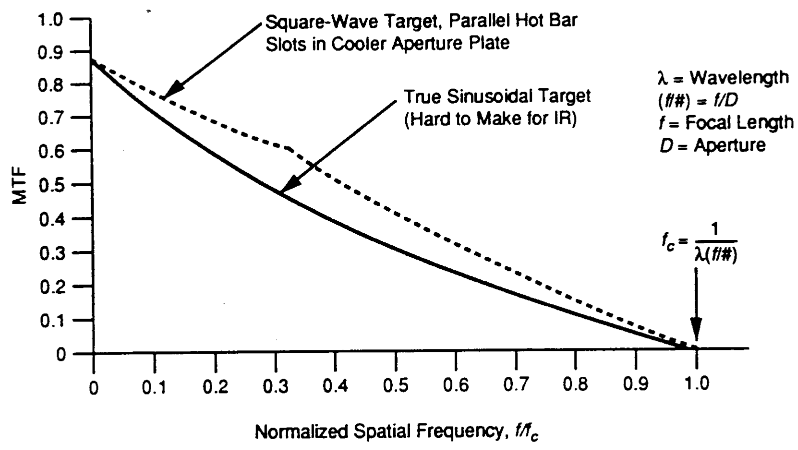

Fig. 1.43 Cutoff frequency for an aberration-free circular aperture (axehead IRLS designs).

2. These Fourier component sinusoidal waves are assumed to be continuous (with no beginning or end). In nature this does not occur. Fortunately, for IRLS analysis we can ignore this requirement.
3. IRLS system elements must be linear in their response to the amplitude variation of their sinusoidal inputs. In an example IRLS we have previously noted several nonlinear response functions, such as
   a. video amplifier saturation (deliberately introduced to compress the video signal dynamic range).
   b. CRT response is nonlinear in the saturation and threshold regions of the S-shaped transfer curve. The central portion, however, can be treated as a linear response. IRLS MTF analysis is applicable to this linear region only.
   c. Film response in film recorders follows a curve called the H&D curve, or density versus log exposure curve, which has a similar threshold region with a linear midrange; hence, the same remarks as b above apply.
   d. Additional dynamic range compression may be done via digital signal processing if such digital image processing is used in the IRLS.

Care must be used in determining the MTF of such processing. Usually one tries to minimize any processing effects on the IFOV frequency (MTF $\approx$ 1).

The concept of *cutoff frequency* f_c is useful. The cutoff frequency is that frequency where MTF = 0. It can be an optical or an electrical cutoff frequency. Figure 1.43 shows an optical cutoff frequency for an aberration-free circular aperture. The abscissa is normalized spatial frequency f/f_c, where f_c is that frequency where MTF first goes to zero. In optics we can have more than one cutoff.

1.5.1 Across-Track MTF Analysis of IRLS Systems

In IRLS analysis of MTF both the ACT (across-track or x) axis and the ALT (along-track or y) axis must be considered. The IRLS is treated as a cascade because of the higher impedance of PV cells. PC cells are noisier but their lower impedance makes it easier to couple the signal to a practical preamplifier. Typical PC HgCdTe detectors have cell impedances as low as 50 Ω, while a PV cell impedance can be hundreds or even thousands of ohms. If the charge from the PV effect can be temporarily stored in a capacitive-type cell that is periodically coupled to a readout preamplifier, the storage device can act as a miniature impedance transformer. Readout arrays of several types, such as a CCD or a CID or various forms of MOSFET array switches have now been applied to PV arrays. In the near-IR band, platinum silicide arrays with silicon readout arrays have provided impressive performance. A large PV array allows the scanner to be operated at a slower scan rate because the required ALT coverage Φ_{ALT} can be achieved even at high V/H values by adding more detectors to the array in the ALT direction. The complexity of extra bias and preamplifiers is minimized by the readout multiplexer (of whatever type). When smaller IRLS scanners are needed for RPVs and pods, these techniques may be used. The lower signal from the smaller aperture is compensated for by the slower scan (longer dwell per IFOV) and by using more detectors per scan. This can be seen in the scan rate equation:

$$\mathrm{N}_{\mathrm{sc}} = \frac{V/H}{\mathrm{n(IFOV)}} \quad \mathrm{scans/s} \ . \tag{1.78}$$

Using n ALT detectors causes increased off-axis aberrations, especially coma. These aberrations can be partially corrected in the scanner optical design. Coma can be roughly estimated in the round-aperture axehead scanners where these large PV arrays might be used. Coma angular diameter d_c is approximately

$$d_c \approx \frac{0.1875u}{(f/\#)^2} \quad \mathrm{rad} \ , \tag{1.79}$$

where u is the field angle between the chief ray to the point of interest in the focal plane and the optical axis and $f/\#$ is the focal length divided by the aperture diameter. Another trade-off results from the defocus effect. The motivation for the extra detectors in the ALT dimension is to keep up with high V/H values in low-altitude operation. The defocus effect prevents any realization of detector-sized resolution when the detectors are sized for the longer slant ranges, as discussed in Secs. 1.2 and 1.3. Their inherent resolution can only be achieved at large scan angles. Falloff of ALT optical resolution as the off-axis angle increases then becomes less of a problem and practical solutions exist. As the scan angle increases from nadir, the outer detectors can be dropped and the center detectors used, as shown in Fig. 1.33.

1.7.2 Detector Dewars

The IR detector/dewar assembly is a costly and important component of any IRLS. Most IRLS dewars are end-looking designs that accept a cold finger from a split-Sterling cryogenic refrigerator. Integral refrigerators are more rugged and several successful designs have been made. Microphonics or IRLS shape restrictions may prohibit their use because they must fit directly on the dewar.

Table 2.1 *(continued)*

Symbol	Nomenclature	Units
η	Detector quantum efficiency	—
η_{cov}	Detector-array coverage efficiency	—
η_{cs}	Cold-shield efficiency	—
η_s	Total FLIR system efficiency	—
η_0	Effective total detector efficiency	—
λ	Wavelength variable	m
λ_1	Detector cuton wavelength	m
λ_2	Detector cutoff wavelength	m
σ	Stefan-Boltzmann constant	$\mathrm{W\ m^{-2}\ K^{4}}$
σ_o	IR optics design blur	mrad
τ_F	System frame time	—
τ_o	Spectral average optics transmission	—
$\tau_o(\lambda)$	IR optics transmission	—

2.2 PRINCIPLES OF OPERATION

2.2.1 Fundamentals of Thermal Imaging

All material objects above absolute zero radiate electromagnetic radiation. The maximum value of this radiation per unit wavelength is given by the Planck blackbody radiation law,

$$M_e(\lambda,T) = \left(\frac{2\pi hc^2}{\lambda^5}\right)\left[\exp\left(\frac{hc}{\lambda kT}\right) - 1\right]^{-1} \quad [\mathrm{W\ m^{-3}}] \ , \tag{2.1}$$

where

c = speed of light in vacuum = $2.997 \times 10^{8}\ \mathrm{m\ s^{-1}}$
h = Planck's constant = $6.626 \times 10^{-34}\ \mathrm{J\ s}$
k = Boltzmann's constant = $1.381 \times 10^{-23}\ \mathrm{J\ K^{-1}}$
T = absolute temperature in kelvins
λ = radiation wavelength in meters.

The radiation of a real object is obtained by multiplying the blackbody radiation term by the spectral emissivity of the object $\varepsilon(\lambda)$:

$$[M_e(\lambda,T)]_{\mathrm{actual}} = \varepsilon(\lambda,T)M_e(\lambda,T) \ . \tag{2.2}$$

Equation (2.2) can be considered a definition of emissivity. Since the energy per photon is known to be (hc/λ), Planck's law in terms of photon flux can be written as

$$M_q(\lambda,T) = \left(\frac{\lambda}{hc}\right)M_e(\lambda,T) \quad [\mathrm{photons\ s^{-1}\ m^{-3}}] \ . \tag{2.3}$$

input function. This two-dimensional impulse response (which may be thought of as a "blurring" effect) completely describes the system's ability to re-create fine detail in the output and quantifies such qualitative descriptions as "resolution." It is common to call the area over which there is significant signal correlation as the resolution area, and this is a useful quantitative measure. Each functional element of a system has its own impulse response, and, from linear system theory, the resultant total system response is found by mathematically convolving these together. But, since the Fourier transform of a convolution is the product of the Fourier transforms of the individual functions, it is easier to work in transform space (spatial frequency in cycles per milliradian) than in real space (milliradians). For this reason the commonly used measure of FLIR system image fidelity is defined to be the (normalized) magnitude of the Fourier transform of the system impulse response function. This ignores phase, which can be important. The rationale here is that, unlike real-time-based systems where there is an inherent relationship between amplitude and phase due to causality, imaging systems are space based. In simple terms, there is no reason to require that an impulse response be zero, in, say, the negative x direction. Phase shifts can be introduced, by asymmetry in the optics or display and in the electronic signal processing. For simplicity we assume any such effects to be negligible and ignore phase in all that follows.

The easiest way to obtain the MTF of any subsystem (or the entire system) is to determine the output resulting from an input "point source." This is an input of spatial, or time, dimension very much smaller than any anticipated output dimension, and of amplitude adjusted to size so as to result in unit area. In the limit of zero size and infinite amplitude this reduces to a Dirac delta function. Then, the Fourier transform of this output function is calculated and its magnitude normalized to unity at zero frequency. This normalized magnitude is the MTF of that element. If the magnitude happens to be zero at zero frequency, as would be the case, for example, for an ac-coupled circuit, or indeterminate, as it may be for a dc-restored circuit, then it is customary to normalize the element MTF so that the maximum value of the total system MTF is unity. In the following we restrict derivations to one dimension for simplicity.

2.3.1.1 Image Formation MTF.

An optical system with a finite-size entrance pupil will image an object-space point source as a specific image-plane power distribution uniquely determined by the size and shape of this entrance pupil. This distribution is called a diffraction pattern. The resulting MTF for monochromatic radiation can be determined by suitably normalizing the convolution of the aperture with itself, and will be different in each dimension if the pupil is not symmetric. The result for a circular aperture is

$$\mathrm{MTF}_{\mathrm{diff}} = \left(\frac{2}{\pi}\right)\left\{\arccos\left(\frac{f}{f_c}\right) - \left(\frac{f}{f_c}\right)\left[1 - \left(\frac{f}{f_c}\right)^2\right]^{1/2}\right\} , \tag{2.20}$$

where f is the spatial frequency variable and

$$f_c = \frac{D_o}{\lambda} . \tag{2.21}$$

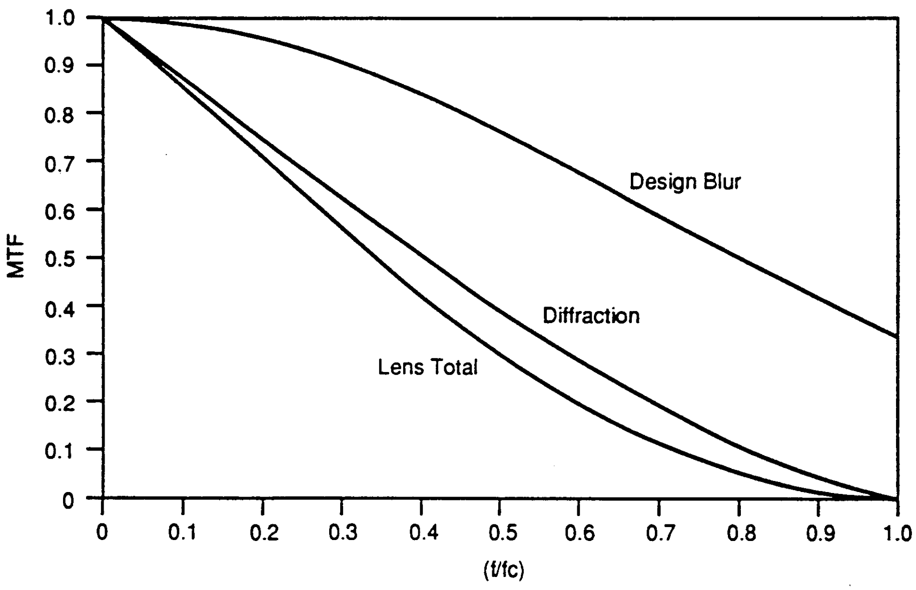

Fig. 2.8 LWIR lens MTF. Design blur σ = IFOV/3. The total lens system MTF is the product of diffraction and geometrical design blur.

As stated previously, IR optical systems are usually diffraction limited, whereas visible systems are usually design blur limited. However, design blur (imperfect geometrical focus) can be a significant factor for FLIR as well. The causes of this are well documented in numerous optics design sources. The result is that the design blur impulse response is approximately a Gaussian shape in two dimensions. The MTF is therefore also Gaussian and is given by

$$\mathrm{MTF}_{\mathrm{design}} = \exp[-\pi(f\sigma_0)^2] , \tag{2.25}$$

where σ_0^2 is the effective Gaussian width squared, defined as 2π times the mean square deviation in mrad^2 and f is the spatial-frequency variable in cycles mrad^{-1}. In summary, the optical system MTF is approximately, assuming perfect symmetry,

$$\mathrm{MTF}_{\mathrm{optics}} = \mathrm{MTF}_{\mathrm{diff}}\mathrm{MTF}_{\mathrm{design}} \tag{2.26}$$

and can be approximated by

$$\mathrm{MTF}_{\mathrm{optics}} \cong \left(1 - \frac{f}{f_D}\right) \exp[-\pi(f\sigma_0)^2] , \tag{2.27}$$

with f_D given by Eq. (2.24). The quantity σ_0 can be regarded as a degradation factor associated with the quality of the optical system materials, design, fabrication, and mounting. The total lens system MTF is shown in Fig. 2.8.

2.3.1.2 Infrared Detection MTF.

It might appear that the resolution effect associated with the primary detection process depends on the type of system, the array format, the signal processing, and the type of display. While it is

2.3.1.3 Signal Processing and Display Effects.

The MTF associated with the signal-processing function is difficult to generalize and usually must be evaluated on a case-by-case basis. Fortunately, it is possible to reduce the degradation here to an insignificant level. The primary factor is the temporal frequency response of the analog circuits, preamps, multiplexers, sample-and-hold circuits prior to analog-to-digital conversion, etc., and this can show up as vertical and/or horizontal MTF loss. A common pitfall is to get lost in the flip-flopping back and forth between vertical and horizontal, and in the time-base relationship to spatial frequency. Frequencies can vary from kHz to many MHz within the same processor, and the spatial correspondence must be carefully determined.

The same considerations apply to the display. If it is a single-beam CRT, as commonly used in any TV standard, the effect is almost entirely attributed to the video channel frequency response and to the electron-beam shape and size. The latter usually dominates and is almost always a Gaussian. In this case, it is equivalent to an optics design blur with its own σ.

2.3.1.4 Composite System MTF.

The total system MTF is the product of the subsystem functions, so

$$\mathrm{MTF}_{\mathrm{system}} = \left(1 - \frac{f}{f_D}\right) \exp[-\pi(f\sigma_0)^2]\left(\frac{\sin \pi f \Delta\theta}{\pi f \Delta\theta}\right)\mathrm{MTF}_{\mathrm{p}}\mathrm{MTF}_{\mathrm{D}} , \tag{2.30}$$

where

f = spatial frequency coordinate in cycles/mrad
f_D = diffraction cutoff frequency in cycles/mrad
$\Delta\theta$ = detector IFOV in mrad
$\mathrm{MTF}_{\mathrm{p}}$ = MTF of the signal processor
$\mathrm{MTF}_{\mathrm{D}}$ = MTF of the display.

This assumes a circular optical aperture. or that an equivalent one can be defined (almost always the case), and is valid only for $f \leq f_c$. Outside this range, the MTF is zero. A typical FLIR system total MTF for LWIR operation is shown in Fig. 2.10. Figure 2.11 indicates the change in MTF for MWIR operations.

The sinc function in Eq. (2.30) has a first zero when its argument is π. This corresponds to a frequency of

$$f = \frac{1}{\Delta\theta} . \tag{2.31}$$

Since this is almost always less than f_D, it is regarded as the useful frequency limit to FLIR performance. A commonly used reference spatial frequency f_0 is defined to be one-half this value, or

$$f_0 = \frac{1}{2\Delta\theta} . \tag{2.32}$$

For a well-designed sensor and a good display, diffraction and detector MTF dominate. At f_0, diffraction is typically 0.7, detector MTF is 0.64, design blur and λ_1, λ_2 describe the integration spectral band.

Detector noise is traditionally specified in terms of its noise equivalent power, NEP, such that the total (wavelength-independent) noise V_n is

$$V_n = R(\lambda)\mathrm{NEP}(\lambda) \ . \tag{2.35}$$

Also, a normalized noise measure D^* is defined to be

$$D^*(\lambda) = \frac{(A_D \Delta f)^{1/2}}{\mathrm{NEP}(\lambda)} \ , \tag{2.36}$$

where Δf is the electrical bandwidth over which the rms noise V_n is measured. Then, using Eqs. (2.33), (2.35), and (2.36), we have, for the signal-to-noise ratio,

$$\frac{S}{N} = \left[\frac{1}{4}\left(\frac{A_D}{\Delta f}\right)^{1/2} (f/\#)^{-2}\right] \int_{\lambda_1}^{\lambda_2} [\Delta M_e(\lambda)\tau_A(\lambda)][\tau_o(\lambda)D^*(\lambda)]\, d\lambda \ . \tag{2.37}$$

Relation (2.37) can be considered sort of a master equation from which all subsequent NET analysis evolves. This analysis can be done in a number of ways, all of which ultimately lead to the same result. We proceed in a special way as follows.

We can interpret S/N as the result of multiplying a source term I_S by a response factor I_R. That is,

$$\frac{S}{N} = I_R I_S \ , \tag{2.38}$$

where

$$I_R = \left[\frac{1}{4}\left(\frac{A_D}{\Delta f}\right)^{1/2} (f/\#)^{-2}\right] \int_{\lambda_1}^{\lambda_2} M_e'(\lambda)\tau_o(\lambda)D^*(\lambda)\, d\lambda \ , \tag{2.39}$$

$$I_S = \frac{\displaystyle\int_{\lambda_1}^{\lambda_2} \tau_A(\lambda)\tau_o(\lambda)D^*(\lambda)\Delta M_e(\lambda)\, d\lambda}{\displaystyle\int_{\lambda_1}^{\lambda_2} M_e'(\lambda)\tau_o(\lambda)D^*(\lambda)\, d\lambda} \ , \tag{2.40}$$

$$M_e'(\lambda) = \left[\frac{\partial M_e(\lambda,T)}{\partial T}\right]_{T=T_0} \ . \tag{2.41}$$

Now, the source term I_S has the units of temperature, so it is natural to define FLIR input signal in terms of an equivalent temperature differential. The response factor I_R must have the units of inverse temperature, so the reciprocal of I_R must be some sort of equivalent temperature noise. We thus define the spot noise NET_s as the reciprocal of I_R.

Then, defining

$$\tau_o = \frac{\int_{\lambda_1}^{\lambda_2} [M_e'(\lambda)D^*(\lambda)]\tau_o(\lambda)\, d\lambda}{\int_{\lambda_1}^{\lambda_2} M_e'(\lambda)D^*(\lambda)\, d\lambda} , \tag{2.42}$$

$$D^*_{\mathrm{BB}} = \left(\frac{1}{4\sigma T_0^3}\right)\int_{\lambda_1}^{\lambda_2} M_e'(\lambda)D^*(\lambda)\, d\lambda , \tag{2.43}$$

we have

$$\mathrm{NET_s} = \left(\frac{\Delta f}{A_D}\right)^{1/2} \frac{(f/\#)^2}{\sigma T_0^3 \tau_o D^*_{\mathrm{BB}}} . \tag{2.44}$$

This is a central result and expresses single-element temperature noise in a generalized standard form. The term defined by Eq. (2.42) is the effective optics transmission, and the term defined by Eq. (2.43) is called the blackbody D^*.

The standard definition of NET is that blackbody temperature difference required to produce an S/N of one, over a reference bandwidth, with unity atmospheric transmission. For a blackbody, unity τ_A, and small ΔT_0, we have

$$I_s = \Delta T_0 , \tag{2.45}$$

where ΔT_0 is the true, thermodynamic temperature difference between the target and its background. Therefore, the standard NET is just the $\mathrm{NET_s}$ defined by Eq. (2.44) evaluated at a reference bandwidth Δf_R. This reference bandwidth is usually defined as

$$\Delta f_R = \left(\frac{\pi}{2}\right)\left(\frac{1}{2t_D}\right) , \tag{2.46}$$

where t_D is the detector dwell time, defined as the time required for it to scan a distance equal to its size in the scan direction. For a scanning system this would be

$$t_D = \frac{\Delta\theta}{V_s} , \tag{2.47}$$

where $\Delta\theta$ is the IFOV and V_D is the element scan speed in milliradians per second. Therefore, by definition, the standard NET for a single detector is

$$\mathrm{NET} = \mathrm{NET_s}\Delta f_R , \tag{2.48}$$

with $\mathrm{NET_s}$ given by Eq. (2.44).

this out and produce a displayed image correctly corresponding to the focal-plane image. The normalized transfer function for the image will be the entire system MTF, and the noise power spectrum can be written as

$$G(f_x,f_y) = G_0 a^2(f_x,f_y) \quad [°\mathrm{C}^2\ \mathrm{mrad}^2] \ , \tag{2.57}$$

where $a(f_x,f_y)$ is the normalized transfer function of all elements following the point of noise insertion. This function is essentially determined by the product of the processor and display MTF. In any event, the integral of a^2 over all spatial frequencies is inversely proportional to the area over which the noise is reasonably correlated, and this area will always be less than the resolution area.

Now, consider the signal-to-noise ratio that would result from averaging over the entire display. For a rectangular display of dimension $\phi_x \times \phi_y$, the transfer function for this averaging process would be

$$\mathrm{TF}(f_x,f_y) = \mathrm{sinc}(\pi f_x \phi_x)\,\mathrm{sinc}(\pi f_y \phi_y) \ , \tag{2.58}$$

so the noise must be

$$\overline{\delta T_F^2} = G_0 \int_{-\infty}^{\infty} \int_{-\infty}^{\infty} a^2(f_x,f_y)\mathrm{TF}^2(f_x,f_y)\, df_x\, df_y \ , \tag{2.59}$$

but TF is so sharply peaked about the origin compared to $a(f_x,f_y)$ for any usable system design that Eq. (2.59) reduces to

$$\overline{\delta T_F^2} = (\phi_x \phi_y)^{-1} G_0 \tag{2.60}$$

for anything that could be considered an imaging system. The display average S/N is then

$$\left(\frac{S}{N}\right)_F^2 = (\phi_x \phi_y)(\overline{\Delta T})^2 G_0^{-1} \ . \tag{2.61}$$

But, from the viewpoint of photon counting, this must be inversely proportional to the total number of background photons counted N_{BT} by all detectors over the entire frame time τ_F. Then, since

$$\Delta N_{\mathrm{ST}} = \sum_{i=1}^{N_1} \left(\frac{\partial N_S}{\partial T}\right) \Delta T_i = N\left(\frac{\partial N_S}{\partial T}\right)\overline{\Delta T} = \left(\frac{\partial N_{\mathrm{ST}}}{\partial T}\right)\overline{\Delta T} \ , \tag{2.62}$$

where ΔN_{ST} is the total signal count. it must be that

$$\left(\frac{S}{N}\right)_F^2 = \eta_D N_{\mathrm{BT}}^{-1} \left(\frac{\partial N_{\mathrm{ST}}}{\partial T}\right)^2 (\overline{\Delta T})^2 \ . \tag{2.63}$$

Thus,

$$\Delta T_A = \Delta T e^{-\beta R} . \tag{2.98}$$

Now, since the aspect ratio for an MRT target is 7:1, one bar subtends an angle of

$$\Delta\phi = \frac{S}{7R} , \tag{2.99}$$

and the target frequency is

$$f = (2\Delta\phi)^{-1} = \left(\frac{3.5}{S}\right)R . \tag{2.100}$$

Then, defining R_0 by

$$R_0 = \frac{S}{7\Delta\theta} , \tag{2.101}$$

we have

$$\frac{f}{f_0} = \frac{\Delta\theta}{\Delta\phi} = \frac{R}{R_0} . \tag{2.102}$$

Therefore, since the temperature required to resolve the target is the MRT at the target frequency, it must be that

$$\Delta T e^{-\beta R} = \mathrm{MRT}\left(\frac{R}{R_0}\right) . \tag{2.103}$$

Relation (2.103) is the fundamental expression for determining recognition range for a given system. This can be done by simultaneously plotting both sides of Eq. (2.103) as a function of R and noting that the intersection is the value of R that makes them equal; this is graphically represented in Fig. 2.16. We note that the factor translating target frequency to range is R_0. That is, in plotting the system MRT curve, stated in terms of f/f_0, we scale the ordinate to range R by

$$R = R_0\left(\frac{f}{f_0}\right) \tag{2.104}$$

and thus anticipate that R_0 will be a dominant factor in determining recognition range.

The graphical procedure described above is only useful in determining the range performance of a specific system. What is needed for trade-off analyses is a closed expression relating range to system parameters. To this end we note that if $a^2(f)$ is a monotonically decreasing function of f, we can approximate MRT by

Table 2.4 Derived System Parameters

Parameter	Relation	Value
$\Delta\theta$	u/fl	0.175 mrad
f_0	$1/2\Delta\theta$	2.86 cycles mrad^{-1}
$(\mathrm{FOV})_y$	$240\Delta\theta$	42.0 mrad
$(\mathrm{FOV})_x$	$320\Delta\theta$	56.0 mrad
A_R	$D_o\Delta\theta$	0.70
η_{cov}	$N\Delta\theta^2/(\mathrm{FOV})_x(\mathrm{FOV})_y$	1.56×10^{-3}
η_s	$\tau_o\varepsilon_s^{1/2}\eta_{\mathrm{cov}}^{1/2}\eta_{\mathrm{cs}}^{1/2}\eta_D^{1/2}$	4.76×10^{-3}
NET_0	[Relation (2.68)]	$4.58 \times 10^{-4}\,{}^\circ\mathrm{C}$
G_0	$(\eta_s D_o)^{-2}\mathrm{NET}_0^2$	$5.79 \times 10^{-5}\ {}^\circ\mathrm{C}^2\ \mathrm{mrad}^2$
NET*	$G_0^{1/2}/\Delta\theta$	0.14°C

$$\mathrm{MTF}_{\mathrm{design}}\left(\frac{f}{f_0}\right) = \exp[-\pi(f\sigma_0)^2] = \exp\left[-0.086\left(\frac{f}{f_0}\right)^2\right] , \tag{2.123}$$

$$\mathrm{MTF}_{\mathrm{det}}\left(\frac{f}{f_0}\right) = \mathrm{sinc}\left[\left(\frac{\pi}{2}\right)\left(\frac{f}{f_0}\right)\right] . \tag{2.124}$$

The product of Eqs. (2.122), (2.123), and (2.124) is shown in Fig. 2.10 labeled as "IR receiver." We next assume that the product of the signal processor and display can be represented by a Gaussian such that the MTF at f_0 is equal to 0.90. That is,

$$\mathrm{MTF}_{\mathrm{display/elec}}\left(\frac{f}{f_0}\right) = \exp\left[-0.10\left(\frac{f}{f_0}\right)^2\right] . \tag{2.125}$$

Equation (2.125) is plotted in Fig. 2.10, labeled "display/elec." The total system MTF, also shown in Fig. 2.10, is then just the product of Eqs. (2.122) through (2.125).

If we ignore the Q factor of Eq. (2.97), we have, for MRT,

$$\mathrm{MRT} = 0.7\left(\frac{f}{f_0}\right)\left[\frac{\mathrm{NET}^*}{\mathrm{MTF}_s(f/f_0)}\right] = 0.098\left[\frac{(f/f_0)}{\mathrm{MTF}_s(f/f_0)}\right] . \tag{2.126}$$

Equation (2.126) is plotted in Fig. 2.14.

Now, for a 2.0-m MRT target, 3°C above ambient, and an atmospheric extinction coefficient of 0.4 km^{-1}, we calculate the following:

$$\alpha = -\ln \mathrm{MTF}_s(1) = -\ln 0.339 = 1.08 , \tag{2.127}$$

$$\gamma = \frac{\Delta T}{0.7\ \mathrm{NET}^*} = \frac{3}{0.098} = 30.6 ; \tag{2.128}$$

4.2.1.1 Radiative Signature Components. A general methodology to estimate target signature radiative components is as follows:

1. Divide the object, including the plume, into elements of surface area A_i small enough such that the temperature and emissivity of each can be assumed constant.
2. By reference to the appropriate phenomenology (plume, aerodynamic heating, etc.) deduce the temperature T_i of each surface element A_i and its respective spectral angular emissivity $\varepsilon_i(\lambda, \theta, \phi)$.
3. Calculate the spectral radiant exitance from each surface element A_i using the Planck expression for graybody emission:

$$W_{\lambda i} = \varepsilon_i(\lambda, \theta, \phi) C_1 \lambda^{-5}\left[\exp\left(\frac{C_2}{\lambda T_i}\right) - 1\right]^{-1} \quad [\mathrm{W\ cm^{-2}\ \mu m^{-1}}] \ , \tag{4.2}$$

where

C_1 = 3.741844×10^4 W cm^{-2} μm^4
C_2 = 1.438769×10^4 μm K
$\varepsilon_i(\lambda, \theta, \phi)$ = directional spectral emissivity
λ = wavelength in microns
T_i = temperature of surface element.

4. Determine the projected area of each surface element A_i' in the direction of the observation. For a diffuse Lambertian emitter $\varepsilon(\lambda, \theta, \phi) = \varepsilon(\lambda)$, where $\varepsilon(\lambda)$ is the hemispherical spectral emissivity.
5. Calculate the radiant intensity from each element in the direction of the receiver:

$$I_i(\lambda) = \frac{W_{\lambda i}}{\pi} A_i' \ . \tag{4.3}$$

6. Sum over all target elements:

$$I_T(\lambda) = \sum_i I_i(\lambda) \ . \tag{4.4}$$

4.2.1.2 Reflected Signature Components. These components are treated in Secs. 4.2.1.8 and 4.2.1.9.

4.2.1.3 Jet Engine Signature Approximations. Jet engines can be divided into three classes: turbojets, turbofans, and ramjets. The total infrared emission from jet engines consists of plume, tailpipe, exhaust nozzle, and cowling components, shown in Fig. 4.8. Estimation of this radiation relies on simple graybody approximations. Typical jet engines meet the conditions required for treatment of the exhaust nozzle component as a graybody cavity, thus reducing all jet engine radiation components to treatment by the steps outlined in Sec. 4.2.1.1. The emissivity ε for the nozzle and tailpipe components can be taken to be 0.9 and to be spectrally independent. The exhaust nozzle component temperature T_e is related to a commonly reported engine parameter known as exhaust gas temperature (EGT) read by thermocouple just aft of the turbine. EGT is a function of airspeed and altitude, and varies from 300 to 900°C for

4.2.2.11 Measured Terrain PSD Data. The data on the following pages* (Figs. 4.60 to 4.97) is presented as a representation of measured background power spectra density functions, including arctic, farm and field, clouds, mountain, ocean and coastline, and urban areas. These data were gathered with the calibrated HICAMP II sensor mounted on NASA U-2 aircraft at a constant altitude of 60,000 ft. PSD data are presented in representative spectral bands in the SWIR 3- to 5-μm band and the LWIR 8- to 12-μm band and are given in terms of "μ flicks" = 10^{-6} W cm^{-2} sr^{-1} μm^{-1}. A correction for the response of the instrument must be made to render these data useful as indicators of the spatial-frequency content of these scenes. The approximate normalized MTFs of the instrument are

$$\mathrm{MTF(SWIR)} = \exp(-1.21 f^2) \tag{4.51}$$

and

$$\mathrm{MTF(LWIR)} = \exp(-1.38 f^2) \ , \tag{4.52}$$

where f is in cycles per milliradian. For f in cycles per kilometer, the constant in the above expression becomes -4.02×10^{-4} and -4.63×10^{-4}, respectively. The instrument's response is relatively constant out to about 20 cycles per kilometer.

---

*Note: On the following pages, the PSD plots in Figs. 4.60 to 4.97 are in error. To correct: (1) divide horizontal scale by 4, (2) ignore all data below 1 cycle/km, and (3) divide vertical scale by 100.

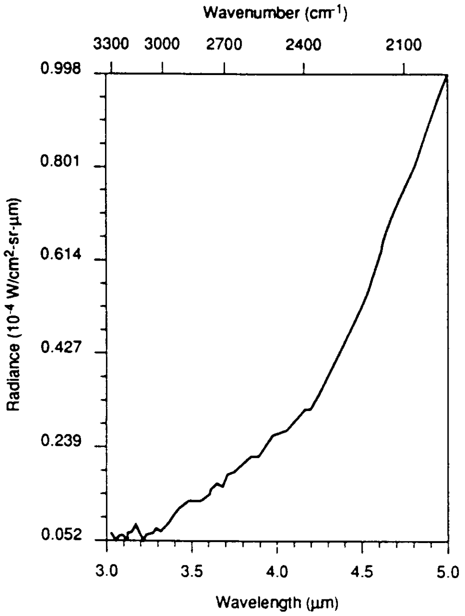

Fig. 4.117 Total horizontal path spectral radiance in the 3- to 5-µm band looking due east at 300-km range, 3-km altitude. 1976 Standard Atmosphere is calculated from LOWTRAN 7. Input conditions are shown in Table 4.4. Average radiance = 6.980×10^{-5} W cm^{-2} sr^{-1} µm^{-1}.

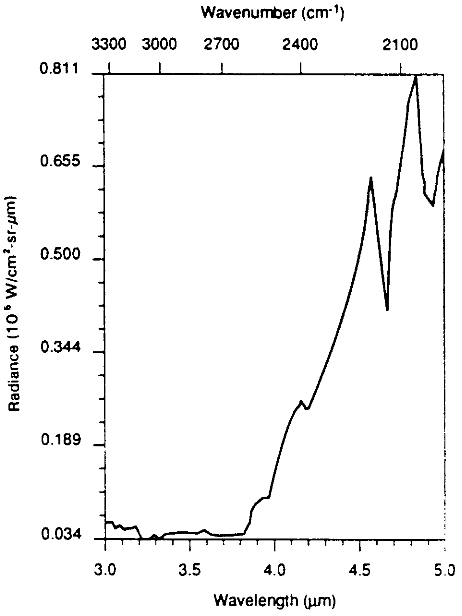

Fig. 4.118 Total horizontal path spectral radiance in the 3- to 5-µm band looking due east at 300-km range, 10-km altitude. 1976 Standard Atmosphere is calculated from LOWTRAN 7. Input conditions are shown in Table 4.4. Average radiance = 5.257×10^{-6} W cm^{-2} sr^{-1} µm^{-1}.

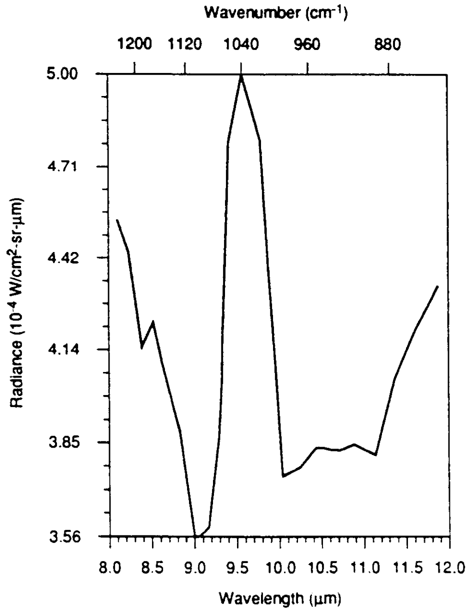

Fig. 4.119 Total horizontal path spectral radiance in the 8- to 12-µm band looking due east at 100-km range, 3-km altitude. 1976 Standard Atmosphere is calculated from LOWTRAN 7. Input conditions are shown in Table 4.4. Average radiance = 1.898×10^{-3} W cm^{-2} sr^{-1} µm^{-1}.

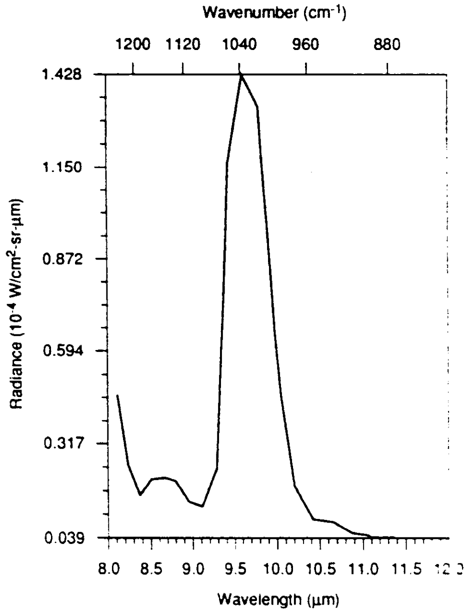

Fig. 4.120 Total horizontal path spectral radiance in the 8- to 12-µm band looking due east at 100-km range, 10-km altitude. 1976 Standard Atmosphere is calculated from LOWTRAN 7. Input conditions are shown in Table 4.4. Average radiance = 1.410×10^{-4} W cm^{-2} sr^{-1} µm^{-1}.

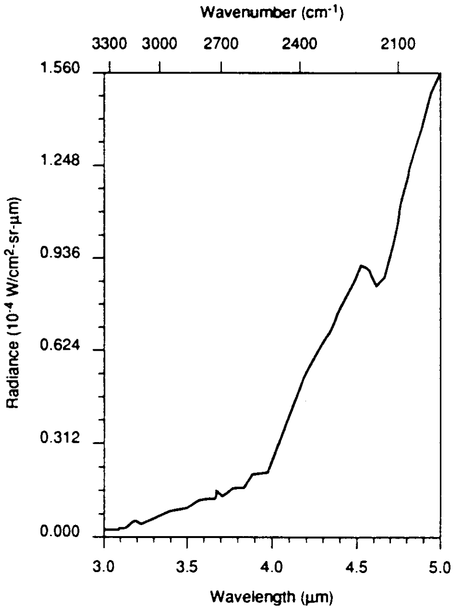

Fig. 4.125 Uplooking scattered path radiance from ground to space in the 3- to 5-µm band. Observer zenith look angle of 85 deg and a solar zenith angle of 0 deg. 1976 Standard Atmosphere is calculated from LOWTRAN 7. Input conditions are shown in Table 4.5. Average band radiance = 9.653×10^{-5} W cm^{-2} sr^{-1} µm^{-1}.

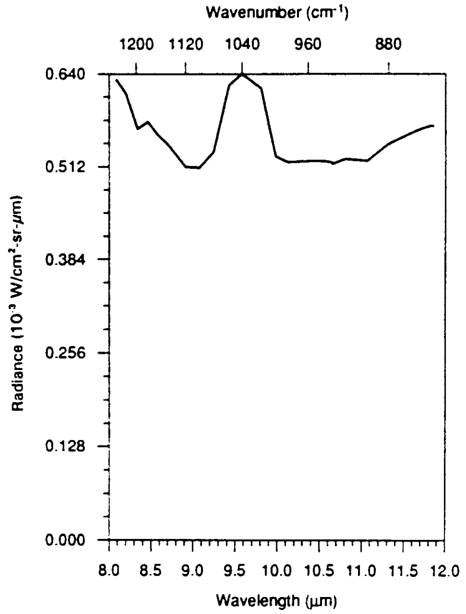

Fig. 4.126 Uplooking scattered path radiance from ground to space in the 8- to 12-µm band. Observer zenith look angle of 85 deg and a solar zenith angle of 0 deg. 1976 Standard Atmosphere is calculated from LOWTRAN 7. Input conditions are shown in Table 4.5. Average band radiance = 6.210×10^{-5} W cm^{-2} sr^{-1} µm^{-1}.

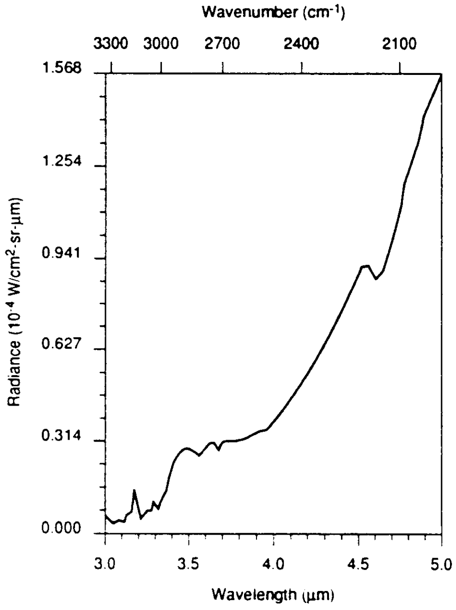

Fig. 4.127 Uplooking scattered path radiance from ground to space in the 3- to 5-µm band. Observer zenith look angle of 85 deg and a solar zenith angle of 45 deg. 1976 Standard Atmosphere is calculated from LOWTRAN 7. Input conditions are shown in Table 4.5. Average band radiance = 1.098×10^{-4} W cm^{-2} sr^{-1} µm^{-1}.

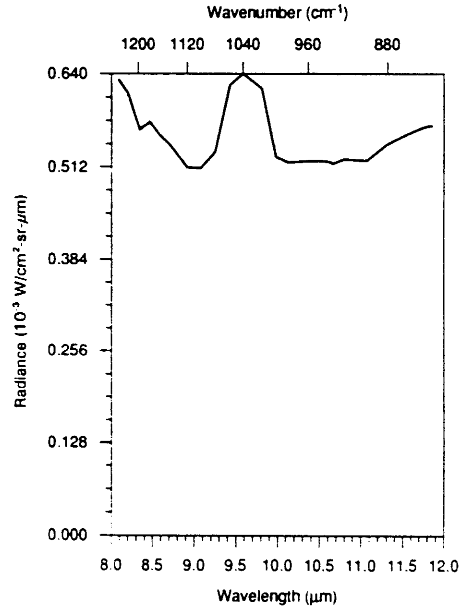

Fig. 4.128 Uplooking scattered path radiance from ground to space in the 8- to 12-µm band. Observer zenith look angle of 85 deg and a solar zenith angle of 45 deg. 1976 Standard Atmosphere is calculated from LOWTRAN 7. Input conditions are shown in Table 4.5. Average band radiance = 7.102×10^{-5} W cm^{-2} sr^{-1} µm^{-1}.

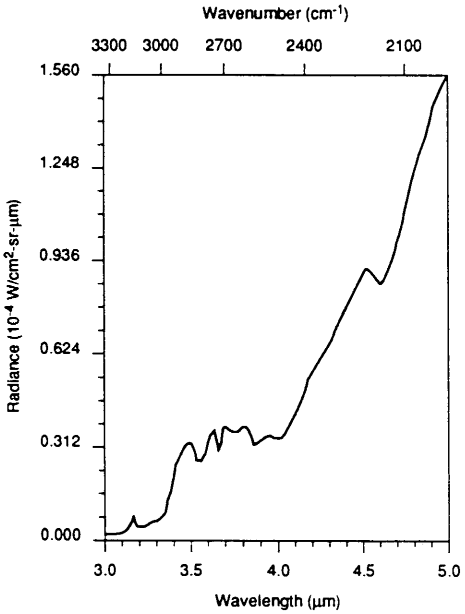

Fig. 4.129 Uplooking scattered path radiance from ground to space in the 3- to 5-µm band. Observer zenith look angle of 85 deg and a solar zenith angle of 85 deg. 1976 Standard Atmosphere is calculated from LOWTRAN 7. Input conditions are shown in Table 4.5. Average band radiance = 1.079 × 10^{-4} W cm^{-2} sr^{-1} µm^{-1}.

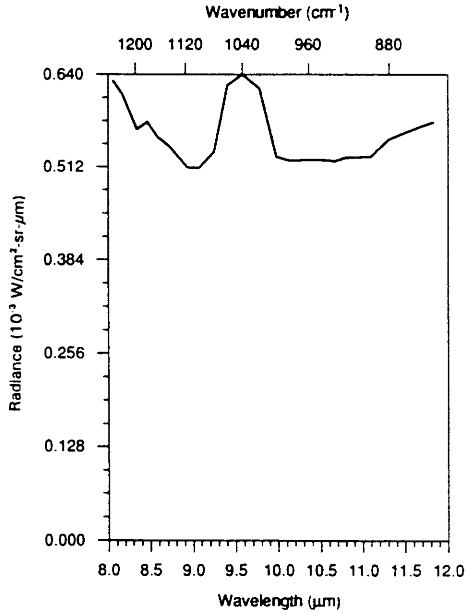

Fig. 4.130 Uplooking scattered path radiance from ground to space in the 8- to 12-µm band. Observer zenith look angle of 85 deg and a solar zenith angle of 85 deg. 1976 Standard Atmosphere is calculated from LOWTRAN 7. Input conditions are shown in Table 4.5. Average band radiance = 5.583 × 10^{-5} W cm^{-2} sr^{-1} µm^{-1}.

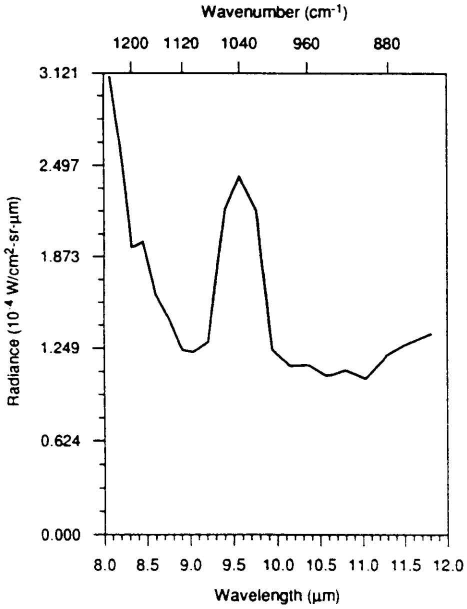

Fig. 4.131 Uplooking scattered path radiance from ground to space in the 3- to 5-µm band. Observer zenith look angle of 30 deg and a solar zenith angle of 0 deg. 1976 Standard Atmosphere is calculated from LOWTRAN 7. Input conditions are shown in Table 4.5. Average band radiance = 5.583 × 10^{-5} W cm^{-2} sr^{-1} µm^{-1}.

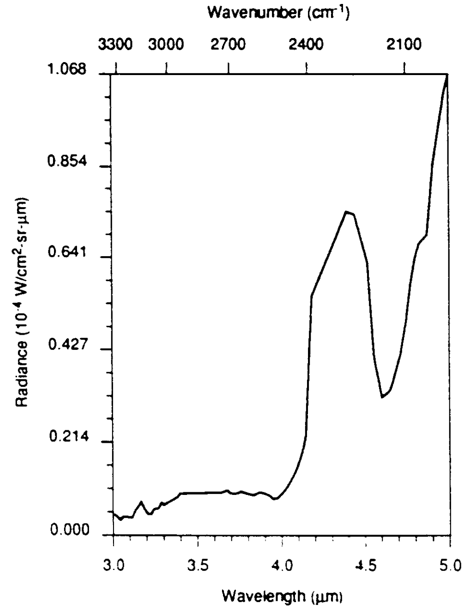

Fig. 4.132 Uplooking scattered path radiance from ground to space in the 8- to 12-µm band. Observer zenith look angle of 30 deg and a solar zenith angle of 0 deg. 1976 Standard Atmosphere is calculated from LOWTRAN 7. Input conditions are shown in Table 4.5. Average band radiance = 7.362 × 10^{-4} W cm^{-2} sr^{-1} µm^{-1}.

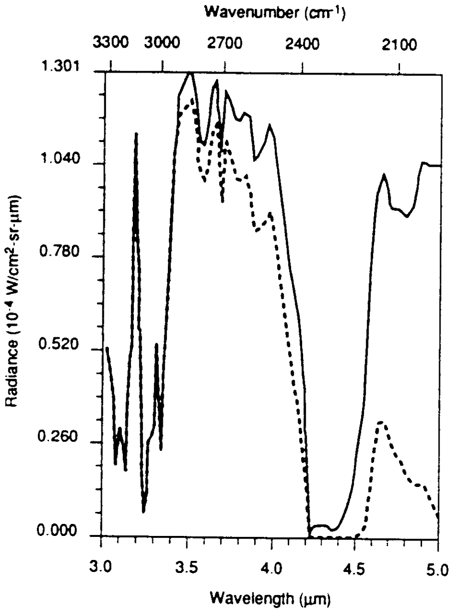

Fig. 4.141 Total downlooking path spectral radiance from space in the 3- to 5-µm band. Solar zenith angle of 0 deg. The dotted line is the contribution from the earth's albedo, ≈ 0.4. Input conditions are shown in Table 4.6. Average band radiance = 1.524 × 10^{-4} W cm^{-2} sr^{-1} $\mu\mathrm{m}^{-1}$.

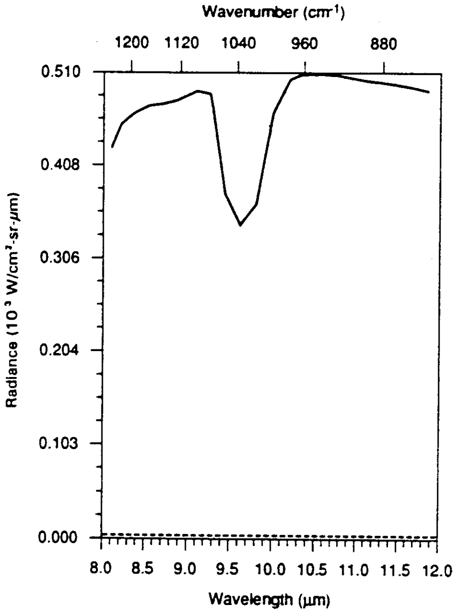

Fig. 4.142 Total downlooking path spectral radiance from space in the 8- to 12-µm band. Solar zenith angle of 0 deg. The dotted line is the contribution from the earth's albedo, ≈ 0.4. Input conditions are shown in Table 4.6. Average band radiance = 2.147 × 10^{-3} W cm^{-2} sr^{-1} $\mu\mathrm{m}^{-1}$.

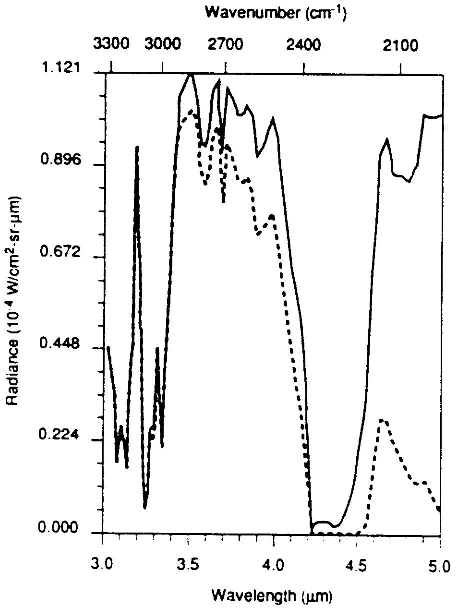

Fig. 4.143 Total downlooking path spectral radiance from space in the 3- to 5-µm band. Solar zenith angle of 30 deg. The dotted line is the contribution from the earth's albedo, ≈ 0.4. Input conditions are shown in Table 4.6. Average band radiance = 1.355 × 10^{-4} W cm^{-2} sr^{-1} $\mu\mathrm{m}^{-1}$.

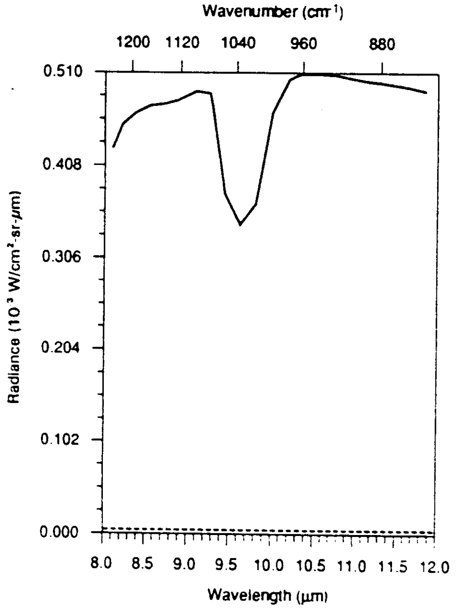

Fig. 4.144 Total downlooking path spectral radiance from space in the 8- to 12-µm band. Solar zenith angle of 30 deg. The dotted line is the contribution from the earth's albedo, ≈ 0.4. Input conditions are shown in Table 4.6. Average band radiance = 2.146 × 10^{-3} W cm^{-2} sr^{-1} $\mu\mathrm{m}^{-1}$.

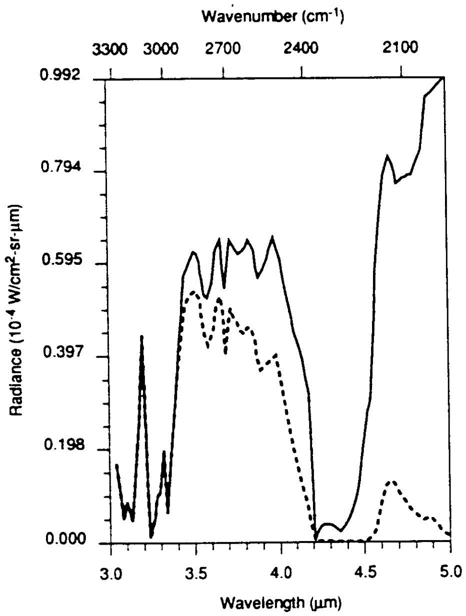

Fig. 4.145 Total downlooking path spectral radiance from space in the 3- to 5-µm band. Solar zenith angle of 60 deg. The dotted line is the contribution from the earth's albedo, ≈ 0.4. Input conditions are shown in Table 4.6. Average band radiance = 9.148 × 10^{-5} W cm^{-2} sr^{-1} μm^{-1}.

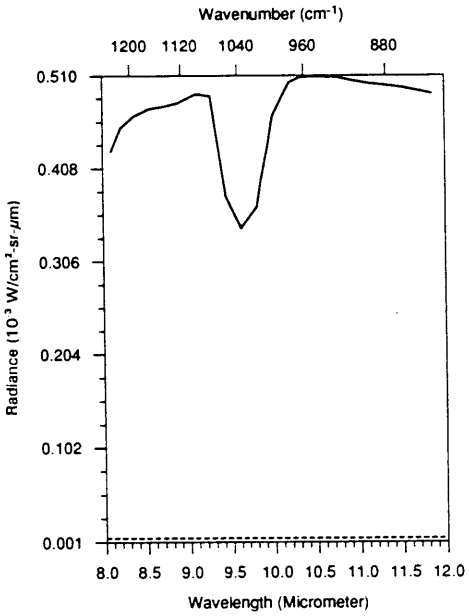

Fig. 4.146 Total downlooking path spectral radiance from space in the 8- to 12-µm band. Solar zenith angle of 60 deg. The dotted line is the contribution from the earth's albedo, ≈ 0.4. Input conditions are shown in Table 4.6. Average band radiance = 2.142 × 10^{-3} W cm^{-2} sr^{-1} μm^{-1}.

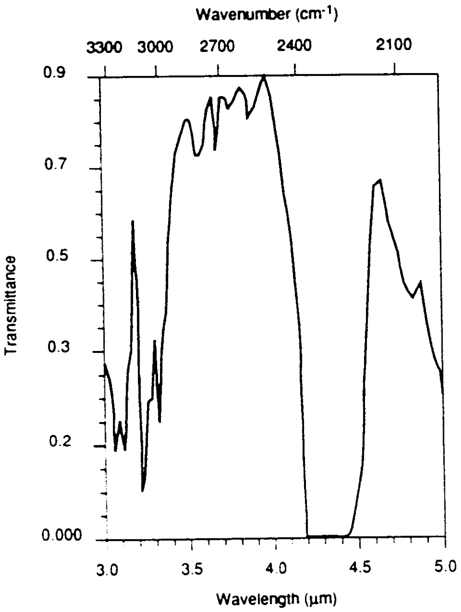

Fig. 4.147 Total downlooking path spectral transmittance from space in the 3- to 5-µm band. 1976 Standard Atmosphere is calculated from LOWTRAN 7. Input conditions are shown in Table 4.6. Average band transmittance = 0.4479.

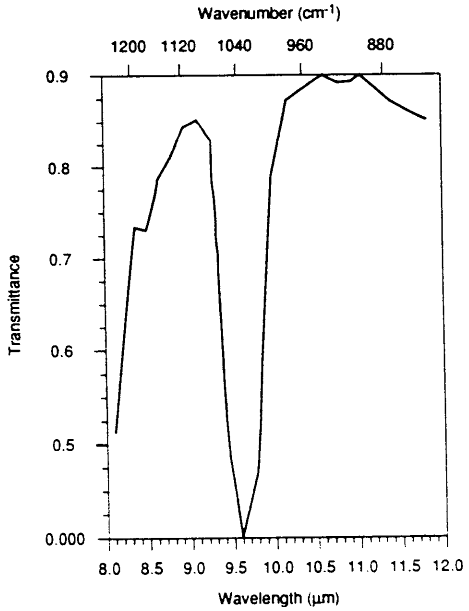

Fig. 4.148 Total downlooking path spectral transmittance from space in the 8- to 12-µm band. 1976 Standard Atmosphere is calculated from LOWTRAN 7. Input conditions are shown in Table 4.6. Average band transmittance = 0.721.

VOLUME 6

The 176.8-dB value computed in Table 3.1(B) for $R_{\max}$ in decibels must be reduced an additional 6.3 dB to account for the atmospheric loss. Thus,

$$R_{\max} \cong (176.8 - 6.3)/4 = 42.63\ \text{dB} \quad \text{or } 18{,}323\ \text{m} .$$

The second iteration assumes a range of 18.3 km, and

$$L_{\text{at}} \cong 0.12 \times 2 \times 18.3 = 4.4\ \text{dB} ,$$

$$R_{\max} \cong (176.8 - 4.4)/4 = 43.1\ \text{dB} \quad \text{or} \quad 20{,}417\ \text{m} .$$

If the loss at 20.4 km, 4.9 dB, is used to compute $R_{\max}$ in a third iteration, $R_{\max}$ equals 19.8 km. No further iterations are necessary because the loss at 19.8 km, 4.8 dB, is very close to the loss assumed. Reference 13 discusses graphic solutions for determining $R_{\max}$ for situations for which the iterative procedure does not converge.

3.2.4 Signal-to-Clutter Computations

Many situations require the detection of targets in a background of distributed clutter. Detection predictions in clutter are less accurate than predictions in noise, because clutter reflectivity is more difficult to model than thermal noise. Distributed clutter may be in a volume or on a surface. The signal-to-clutter ratio (SCR) is the ratio of the target radar cross section (RCS) σ to the clutter RCS σ_c in a resolution cell:

$$\text{SCR} = \frac{\sigma}{\sigma_c} . \tag{3.24}$$

Section 3.3.1 discusses RCS.

3.2.4.1 Volume Clutter. Volume clutter results from the presence of rain, snow, hail, fog, or chaff in a volume. The total clutter RCS of the volume is the product of the reflectivity per unit volume η and the volume V:

$$\sigma_c = \eta V . \tag{3.25}$$

The units of η are square meters per cubic meter. The volume V is

$$V = \frac{\pi}{4}\theta_a\theta_e R^2\rho_r , \tag{3.26}$$

as shown in Fig. 3.9, where R is the range and ρ_r is the range resolution. The azimuth and elevation beamwidths, θ_a and θ_e, to use in Eq. (3.26) are approximately 75% of the −3-dB one-way beamwidths.[13] Section 3.3.3 discusses the volume backscatter coefficient η.

3.2.4.2 Surface Clutter. The parameter σ_0 (sometimes written σ^0) is the average reflectivity of distributed clutter on a surface. The clutter RCS σ_c for a surface is the product of σ_0 and the illuminated area A:

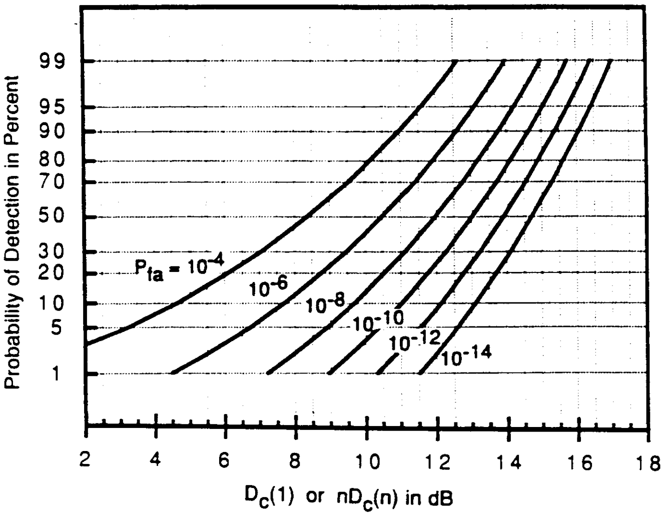

Fig. 3.13 Detectability factor for coherent detection and a nonfluctuating target.

Probability of detection computations made with this empirical formula are within 0.2 dB of those made with more accurate formulas for nonfluctuating targets; consequently, Barton's empirical approach is adequate for most engineering purposes. When there is integration after envelope detection, the required SNR per pulse decreases, but there is an increase in the detector loss, and the full benefit of the increased total energy ratio is not obtained. The additional loss occurring during detection is called the *integration loss* $L_i(n)$, which represents the decrease in efficiency of noncoherent integration compared with coherent integration:

$$L_i(n) = \frac{nD_0(n)}{D_0(1)} = \frac{n}{G_i(n)} \; . \tag{3.44}$$

Figure 3.14 plots $L_i(n)$ versus the number of pulses integrated with $D_0(1)$ as a parameter. Figures 3.12 and 3.14 provide sufficient information to permit the radar designer to calculate the required single-pulse detectability factor when n pulses are integrated noncoherently. Barton's equations also provide the probability of detection when the SNR is known. The coherent detectability factor can be expressed as a function of SNR using Eqs. (3.42) and (3.43).

$$D_C(1) = \frac{n(\mathrm{SNR})^2}{\mathrm{SNR} + 2.3} \; . \tag{3.45}$$

The probability of detection can then be found from Fig. 3.13. For instance, if the single-pulse SNR = 3.16 (5 dB), and 20 pulses are integrated,

$$\alpha = \frac{1.18}{B_3} , \tag{3.57}$$

where B_3 is the half-power width of the spectrum.

When measurements are made with a noncoherent pulse train of n pulses, and there is a mismatch loss

$$\delta f = \frac{1}{\alpha^*[2n(\mathrm{SNR})_1]^{1/2}} , \tag{3.58}$$

where α^* is slightly less than α because of the reduced measurement precision, and $(\mathrm{SNR})_1$ is the single-pulse SNR achieved. For measurements on a coherent pulse train, the effective signal duration for use in Eq. (3.55) is

$$\alpha = 1.81 t_0 , \tag{3.59}$$

where t_0 is the length of the pulse train.

3.2.6.3 Angular Measurement Accuracy.

It can be shown that the minimum rms angular error $\delta\theta$ in the presence of noise is

$$\delta\theta = \frac{K^* \theta_B}{(2E/N_0)^{1/2}} , \tag{3.60}$$

where K^* is a constant that depends on the aperture distribution and θ_B is the -3-dB antenna beamwidth. Table 3.4 lists values of K^* for a number of aperture distributions. The rms angular error for a tracking radar is[23]

$$\delta\theta = \frac{k_1 \theta_B}{k_s[B_T(\mathrm{SNR})(f_r/\beta_s)]^{1/2}} , \tag{3.61}$$

where

k_1 = a constant
k_s = angular error detection slope
SNR = SNR per pulse
f_r = pulse repetition frequency

Table 3.4 Angular Measurement Constants

Aperture Distribution $\lvert x \rvert < D/2$		K^*
Uniform	$A(x) = 1$	0.628
Parabolic	$A(x) = 1 - 4x^2/D^2$	0.936
Cosine	$A(x) = \cos(\pi x/D)$	0.734
Triangular	$A(x) = 1 - 2\lvert x \rvert/D$	0.793

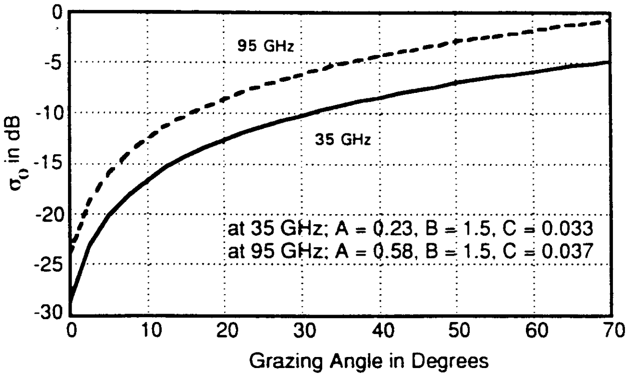

Fig. 3.42 Average σ_0 for wet snow.

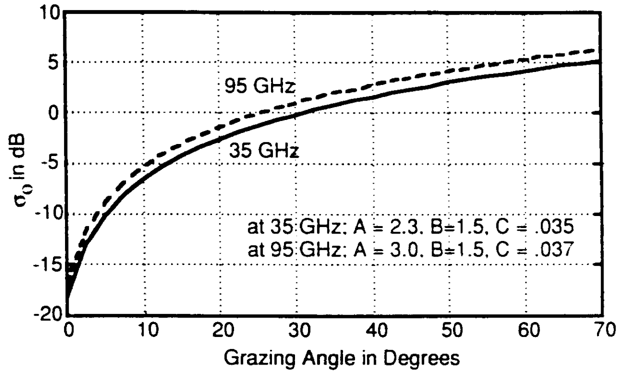

Fig. 3.43 Average σ_0 for dry snow.

model.[68] There is considerable variability in σ_0 with snow measurements, and the values in Figs. 3.42 and 3.43 are somewhat higher than similar data in Ref. 70.

Example. Find the average radar cross section of tree clutter for a 95-GHz radar with resolution cell area A of 10 m^2 at a grazing angle of 20 deg. From Fig. 3.41, the mean value of σ_0 for tree clutter at 95 GHz at $\psi = 20$ deg is -11 dB or 0.079. From Eq. (3.105),

$$\sigma = \sigma_0 A = 0.079 \times 10 = 0.79 \text{ m}^2 \ .$$

In terms of decibels relative to 1 m^2,

$$\sigma = 10 \log(0.79) = -1 \text{ dBsm} \ .$$

Spatial Clutter Variations. The classical approach to the analysis of distributed targets assumes that the backscattered field at the radar antenna (in

Table 3.11 Clutter-to-Noise Ratio Computations at 35 GHz

$\beta_a = 3.43 \times 10^{-3}$ rad, $V = 250$ m/s				
	Parameter	Value	dB+	dB−
P_t	Peak power	10,000 W	40.0	
$G(\psi)^2$	Antenna gain squared	2 × 41.4 dB	82.8	
λ^2	Wavelength squared	$(0.00857)^2$		41.3
σ_c	Clutter cell RCS	−0.20 dBsm		0.2
$(4\pi)^3$				33.0
R^4	Range to fourth power	$(10{,}000)^4$ m^4		160.0
kT_0 deg	Boltzmann's const. × 290	−204 dB (J)	204.0	
F	Noise figure	7 dB		7.0
B	Bandwidth	30 MHz		74.8
L_M	Microwave losses	4 dB		4.0
L_{at}	Atm. losses	0.1 dB/km × 20 km		2.0
		Totals	326.8	322.2
CNR_1 = single-pulse CNR = 326.8 − 322.2 = 4.6 dB				
Number of Pulses Integrated				
$n = \frac{\beta_a \text{RPRF}}{V} = \frac{3.43 \times 10^{-3} \times 10^4 \times 5000}{250} = 686$				
Integration Gain				
$G_i(n) = \frac{n(\text{CNR}_1)}{2(\text{CNR}_1 + 2.3)} \left\{ 1 + \left[1 - \frac{9.2(\text{CNR}_1 + 2.3)}{n(\text{CNR}_1)^2} \right]^{1/2} \right\}$				
$G_i(n) = \frac{686 \times 2.9}{2(2.9 + 2.3)} \left\{ 1 + \left[1 + \frac{9.2(2.9 + 2.3)}{686 \times 2.9^2} \right]^{1/2} \right\} = 25.8 \text{ dB}$				
Integrated Clutter-to-Noise Ratio CNR_{int}				
$(\text{CNR})_{\text{int}} = (\text{CNR})_1 + G_i(n) = 4.6 + 25.8 = 30.4$ dB				

$$\beta_d \cong \frac{2.5\lambda}{R\beta_a} \cong \frac{2.5L}{R} . \tag{3.150}$$

Equation (3.150) assumes that the range resolution is much finer than the azimuth resolution and that the clutter patch becomes decorrelated when more than 20% of the scatterers undergo a phase shift of π radians. With the 3-m aperture, the decorrelation angle is 0.75 mrad at a 10-km range; consequently, there are about 4.6 and 1.7 independent clutter samples at 35 and 95 GHz when the radar flies past the clutter patch at a 10-km range.

The noncoherent integration gain is approximated by the gain for a nonfluctuating target because the fluctuation in the clutter cross section is expected to be small, and because it would be difficult to model and account for the fluctuation. Urkowitz[123] has developed an expression for the integration gain

Table 3.12 Clutter-to-Noise Ratio Computations at 95 GHz

$\beta_a = 1.264 \times 10^{-3}$ rad, $V = 250$ m/s

	Parameter	Value	dB+	dB−
P_t	Peak power	10,000 W	40.0	
$G(\psi)^2$	Antenna gain squared	2 × 45.7 dB	91.4	
λ^2	Wavelength squared	$(0.00316)^2$		50.0
σ_c	Clutter cell RCS	2.3 dBsm	2.3	
$(4\pi)^3$				33.0
R^4	Range to fourth power	$(10{,}000)^4$ m^4		160.0
kT_0 deg	Boltzmann's const. × 290	−204 dB (J)	204.0	
F	Noise figure	8 dB		8.0
B	Bandwidth	30 MHz		74.8
L_M	Microwave losses	7 dB		7.0
L_{at}	Atm. losses	0.5 dB/km × 20 km		10.0
		Totals	337.7	342.8

CNR_1 = single-pulse CNR = 337.7 − 342.8 = −5.1 dB

Number of Pulses Integrated

$$n = \frac{\beta_a \text{RPRF}}{V} = \frac{1.264 \times 10^{-3} \times 10^4 \times 5000}{250} = 253$$

Integration Gain

$$G_i(n) = \frac{n(\text{CNR}_1)}{2(\text{CNR}_1 + 2.3)} \left\{ 1 + \left[1 - \frac{9.2(\text{CNR}_1 + 2.3)}{n(\text{CNR}_1)^2} \right]^{1/2} \right\}$$

$$G_i(n) = \frac{253 \times 0.31}{2(0.31 + 2.3)} \left\{ 1 + \left[1 + \frac{9.2(0.31 + 2.3)}{253 \times 0.31^2} \right]^{1/2} \right\} = 15.6 \text{ dB}$$

Integrated Clutter-to-Noise Ratio CNR_{int}

$(\text{CNR})_{\text{int}} = (\text{CNR})_1 + G_i(n) = -5.1 + 15.6 = 10.5$ dB

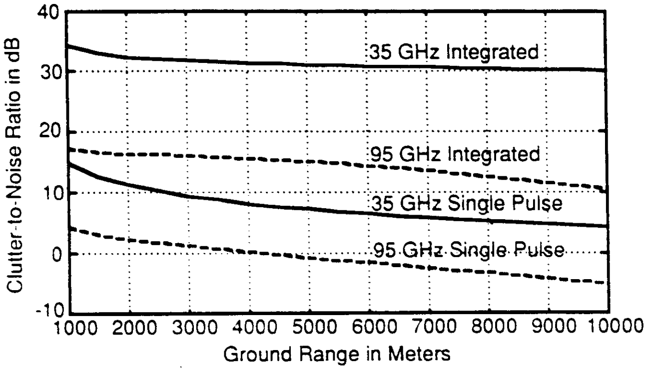

Fig. 3.81 Clutter-to-noise ratio versus ground range with clear air (grass and crop clutter model from Fig. 3.40).

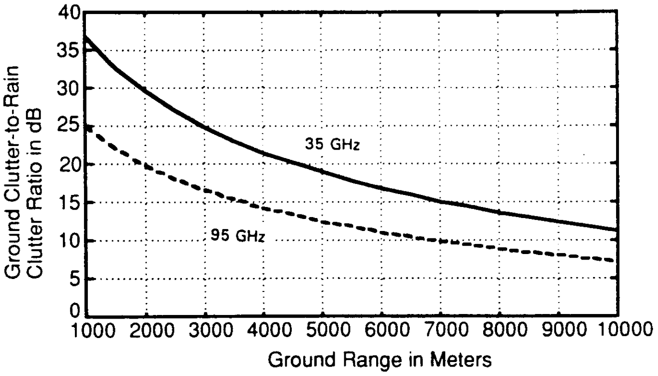

Fig. 3.84 Ground clutter-to-rain clutter ratio with 1 mm/h of rain (grass and crop clutter model from Fig. 3.40).

and Fig. 3.84 shows plots of the ratio of the ground clutter cross section σ_c to the rain backscatter cross section σ_B. Because σ_B is proportional to R^2, and σ_c is proportional to R, the ratio decreases significantly with range. The 95-GHz system cannot make useful ground maps with 1 mm/h of rain because the CNR is too low (see Fig. 3.83); consequently, the low ratio of ground clutter to rain clutter is of no importance at that frequency. With higher rain rates, however, the rain backscatter reduces map contrast at the longer ranges at 35 GHz.

3.5.2.5 Trade-Off Summary. The CNR of the 35-GHz system was better than that of the 95-GHz system with both clear air and 1 mm/h of rain; the CNR of the 95-GHz system was too low for ground mapping in the 1 mm/h rain. The improved azimuth resolution of the 95-GHz system resulted in a higher SCR only at ground ranges less than 4700 m with the grass and crop clutter models. The SCRs were marginal for tank detection at both frequencies. Higher rain rates significantly reduce map contrast at 35 GHz.

3.5.3 Seekers and Munition Guidance

3.5.3.1 Background. One millimeter-wave radar application that has great potential is the radar seeker for smart weapons. Smart weapons include sensor-fused munitions that detect the target and fire a warhead and terminally guided munitions, where the radar sensor searches an area, detects a target, and guides the missile until it hits the target, or is close enough to fire a warhead. There are no civilian applications for missile seekers, and complete descriptions of current systems are not available in the open literature. Missile applications include air to air, air to surface, surface to air, and surface to surface; there are beam-rider, semiactive, and autonomous guidance systems.[124] With a beam-rider system, the missile senses its position in a narrow beam aimed at the target and follows the beam until impact. With semiactive guidance, a separate radar illuminates the target, and the missile homes on the reflected energy. An autonomous system can be active or passive: active systems radiate signals and home on the reflected energy, whereas passive